Filament structure and subcellular organization of the bacterial intermediate filament-like protein crescentin

Yue Liu[1, a], Fusinita van den Ent[1], Jan Löwe[1, *]

AFFILIATIONS:

[1]MRC Laboratory of Molecular Biology, Francis Crick Avenue, Cambridge CB2 0QH, UK

[a] Present address: Department of Microbiology and State Key Laboratory for Diagnosis and Treatment of Infectious Diseases of the First Affiliated Hospital, Zhejiang University School of Medicine, Hangzhou, Zhejiang 310058, China.

* Correspondence: Jan Löwe, MRC Laboratory of Molecular Biology, Cambridge Biomedical Campus, Francis Crick Avenue, Cambridge CB2 0QH, UK, email: jyl@mrc-lmb.cam.ac.uk

KEYWORDS: CreS, cell shape, filamentous proteins, bacterial cytoskeleton, cryo-EM, tomography

CLASSIFICATION: Biological Sciences, Biophysics and Computational Biology

ABSTRACT

The coiled coil protein crescentin is required for the crescent shape of the freshwater bacterium *Caulobacter crescentus* (*vibrioides*). Crescentin forms a filamentous structure on the inner, concave side of the curved cells. It shares features with eukaryotic intermediate filament (IF) proteins, such as its ability to form filaments *in vitro*, the protein's length, sequence comparisons and the presence of a coiled coil discontinuity called the "stutter". Here, we have used electron cryomicroscopy (cryo-EM) to determine the structure of the full-length protein and its filament, exploiting a crescentin-specific nanobody. The filament is formed by two strands, related by two-fold symmetry that each consist of two dimers, resulting in an octameric assembly. Crescentin subunits form longitudinal contacts head-to-head and tail-to-tail, making the entire filament non-polar. Using *in vivo* site-directed cysteine crosslinking we demonstrated that contacts observed in the *in vitro* filament structure exist in cells. Electron cryotomography (cryo-ET) of cells expressing crescentin showed filaments on the concave side of the curved cells, close to the inner membrane, where they form a band. Comparison of our crescentin filament structure with current models of IF proteins and their filaments revealed similar coiled coil dimer formation as well as an absence of overall polarity. IF proteins form head-to-tail longitudinal contacts in contrast to crescentin and hence several inter-dimer contacts in IFs have no equivalents in crescentin filaments. Our work supports the idea that intermediate filament-like proteins achieve their shared polymerization and mechanical properties through a variety of filament architectures.

SIGNIFICANCE STATEMENT

Crescentin is a coiled coil protein that is required for the crescent cell shape of bacteria such as *Caulobacter crescentus*. Crescentin shares biochemical and cytoskeletal properties with intermediate filament (IF) proteins, which form the third major class of cytoskeletal proteins in eukaryotes. To better understand the relationship between crescentin and IF proteins, and the filaments they form, we have determined the three-dimensional structure of crescentin filaments by cryo-EM. This revealed the full-length structure of the parallel coiled coil dimer of crescentin and how dimers come together laterally and longitudinally, to form a non-polar, octameric filament. Differences in filament architecture highlight the versatility of intermediate filament-like proteins across the tree of life.

INTRODUCTION

Fitness of bacteria in the environment is often dependent on their shape. It is therefore that most bacteria tightly control their shape, producing spheres (cocci), rods (bacilli), helices, filaments and irregular, appended as well as crescent shapes [1]. In many cases, shape is dependent on the stress-bearing cell wall. Hence shape determination is dependent on the ability to regulate cell wall synthesis and remodelling during vegetative growth, as well as during cell division [2].

Caulobacter crescentus (*vibrioides*) is crescent shaped. The Gram-negative freshwater bacterium has been studied extensively, and not only because its cells undergo a developmental transition from swarmer to stalked cells. The larger stalked cells are able to attach to surfaces via the stalk, while the swarmer cells are flagellated and motile. Only stalked cells replicate DNA and divide. Their cell division is asymmetric and leads to one swarmer cell and one stalked cell, closing the cell cycle [3]. Both cell types are crescent-shaped. It is thought that the crescent shape is advantageous for cell mobility in their aqueous environment, but it has recently been suggested that the crescent shape enables pili on the swarmer cells to attach to surfaces for biofilm formation [4].

Whatever the biological reason for its crescent shape, in *Caulobacter* it is dependent on the function of the protein crescentin (CreS) [5]. Immunofluorescence and fluorescent protein-tagging using a merodiploid strain (because CreS-GFP fusions were non-functional) showed crescentin to form a single filamentous structure on the inner (concave) surface of the cell crescent [5-7]. The proximity of the crescentin structure to the cell membrane was lost during treatment with the MreB inhibitor A22 or the cell wall inhibitors mecillinam and phosphomycin [6]. Based on the cellular localization, the cytoskeletal properties of crescentin and modelling it has been proposed that its mode of action to create cell shape is mechanical [6]. The finding that MreB is involved [7] might indicate that crescentin filaments reduce cell wall synthesis on one side of the cell, leading to the crescent shape. In line with these ideas, it was found that the heterologous expression of crescentin in *E. coli* leads to curved cells [6], suggesting a conserved or very simple mechanism of cell wall synthesis inhibition.

Crescentin levels in cells do not vary much during the cell cycle [7]. Crescentin filaments in cells are not dynamic and free molecules are added to the filamentous cellular structure rapidly, indicating strong cooperativity of assembly [7, 8]. Initial assembly starts with a cell-long thin structure that thickens as the cell progresses through the cell cycle. Re-arrangements of the crescentin structure occur during cell division, although it is not known how those are regulated or facilitated [7].

The discovery of crescentin as a regulator of cell shape attracted a lot of attention also because of a number of similarities to eukaryotic intermediate filament proteins (IFs) [5, 9]. IFs are the third major class of intracellular filaments in eukaryotes, in addition to microfilaments (actin) and microtubules (tubulin). IFs can be categorized into five major families and include two types of

87 cytoplasmic keratins, vimentin and neurofilament, as well as nuclear lamins [10]. IFs have a well-
88 defined domain architecture, with a central α-helical “rod” domain driving the formation of parallel
89 coiled coil dimers. The rod domain, which has been sub-divided into three coiled coil segments
90 (coil 1A, 1B and 2) and two inter-connecting linkers (L1 and L12), is complemented primarily by
91 disordered head and tail domains (in contrast, nuclear lamins and invertebrate cytoplasmic IFs
92 have folded Ig-fold tail domains). Cytoplasmic IFs have rod domains of about 308 residues, nuclear
93 lamins of about 350 residues. All IF sequences have a “stutter” in the third rod segment that
94 deviates from the regular coiled coil heptad repeat pattern. Despite many years of research there
95 is still no complete structural description of any IF filament [11]. They are known to form tetramers
96 through inter-dimer interactions mediated by their N-terminal regions of the rod domain (“A11”
97 inter-dimer contact). Filaments are thought to contain tetramers as building blocks, at least for the
98 cytoplasmic IFs, and three other types of inter-dimer contacts (“A22”, “A12”, and ”ACN") then lead
99 to higher-order structures such as the prototypical 10 nm-thick mature fibres of many IF proteins
100 [12].

101 Crescentin contains the heptad repeats needed to form an extended coiled coil dimer, and also a
102 stutter in the C-terminal half. The rod domain of crescentin is longer than IF proteins, and it was
103 demonstrated early on that crescentin forms very stable filaments *in vitro* [5]. Filament formation
104 *in vitro* and *in vivo* showed that the domain organization of crescentin is important for its
105 polymerization and cell shape maintenance functions [9]. In particular, membrane attachment was
106 shown to depend on the first 27 amino acids [6, 9]. Removal of the stutter also interfered with
107 crescentin’s ability to curve cells [9].

108 Given the enigmatic relationship between crescentin and IFs, our lack of understanding how
109 crescentin filaments form in cells and how they control cell shape, we set out to understand the
110 crescentin filament structure. We employed electron cryomicroscopy (cryo-EM) on crescentin
111 filaments bound by a newly developed megabody [13] to determine their structure, which revealed
112 an “octameric” twisted and double-stranded filament without polarity. We used *in vivo* site-specific
113 cysteine crosslinking to demonstrate that many, if not all features of the *in vitro* filament structure
114 exist in crescentin filaments in cells. Electron cryotomography (cryo-ET) of *Caulobacter* cells
115 expressing crescentin showed the filaments on the inner, concave side of cells, close to the inner
116 membrane where they form a single, wide band. Comparison with current models of IF proteins
117 revealed significant differences between their filament architectures.

118 **RESULTS**

119 **Development of a megabody for CreS structure determination**

120 In line with previously reported assembly properties of crescentin (CreS) and of many eukaryotic
121 IF proteins [5, 9, 12, 14-16], polymerization of purified, un-tagged *Caulobacter crescentus*
122 *(vibrioides)* CreS upon a decrease of pH *in vitro* led to CreS aggregates, bundles, or irregular
123 filaments that exhibited structural polymorphism. In some cases, cryo-EM micrographs of wild-type
124 (wt) CreS, namely $CreS_{wt,}$ polymerized at pH 7.0 showed unbundled filaments with a width of ~9
125 nm (**Fig. S1A**). Two-dimensional (2D) class averages revealed two intertwined strands with a
126 regular spacing of ~57 nm (distance between helical crossovers) (**Fig. S1B**). Nevertheless, the
127 smooth appearance of these filaments prevented determination of the register of individual
128 subunits along the filament axis.

129 To facilitate structure determination of CreS, we raised nanobodies (NBs) against purified $CreS_{wt}$
130 and selected NBs that bind to $CreS_{wt}$ polymers formed at low pH conditions (**Materials and**
131 **Methods**). Coiled coil prediction [17] and three-dimensional (3D) structure prediction by AlphaFold
132 2 (AF2) [18] **(Fig. S1C)** indicated that CreS contains a central, coiled coil "rod" domain (residues
133 80-444), flanked by an N-terminal segment (residues 1-79, although somewhat shorter in AF2
134 predictions, **Fig. S1C**) and a C-terminal segment (residues 445-457) (**Fig. 1A**). Given the
135 elongated nature of the CreS coiled coil dimer, we engineered an NB derivative, megabody (MB),
136 to act as a bulky and rigid marker bound to CreS. For each NB investigated, a MB was generated
137 by grafting the NB onto a circular permutant of the scaffold protein *E. coli* YgjK, as previously
138 described [13]. Among the MBs, megabody 13 (MB13), a derivative of nanobody 13 (NB13) binds
139 to both $CreS_{wt}$ and $CreS_{sat}$ at pH 8. $CreS_{sat}$ contains a stretch of three amino acids (Ser, Ala and
140 Thr; SAT), inserted before residue 406, to remove the "stutter" that locally disrupts the continuity
141 of the heptad-repeat coiled coil [9, 19] (**Figs. 1B-C and S1D-E**). Cryo-EM analysis revealed that
142 for both versions of CreS, purified CreS-MB13 complex at pH 8 polymerizes into regular,
143 unbundled filaments upon lowering the pH to 6.5 in the presence of detergents, such as CHAPS
144 (**Fig. 1D**). These filaments showed a regular spacing of ~57 nm between neighbouring "nodes",
145 where a node is a segment of the CreS filament decorated with multiple MB13 molecules (**Figs.**
146 **1E and S3A**).

147 For cryo-EM structure determination of CreS, we treated nodes as single particles, using a box
148 size of ~420 Å (henceforth referred to as "small box"), to obtain well-resolved reconstructions of
149 CreS bound with NB13 molecules (**Materials and Methods, Table S3, Fig. S2**). We next extended
150 the box size to ~960 Å (referred to as "large box") for the visualization of a more complete CreS
151 structure, which included regions that are distant from the NB13 binding site, which was mapped
152 to a segment near the C-terminus of CreS (**Materials and Methods, Fig. 2A, Table S3, Fig. S2**).
153 The best small box and large box reconstructions were of $CreS_{sat}$ complexed with NB13,
154 determined at nominal resolutions of 3.34 Å (3.79 Å against the fitted atomic model) and 4.11 Å

155 (4.75 Å against the fitted atomic model), respectively (**Fig. S3B-E, Table S3**). The register of
156 individual amino acids on $CreS_{sat}$ was assigned based on the binding site of NB13 on CreS and
157 the observed patterns of well-resolved side chain densities (**Materials and Methods, Figs. S3B**).
158 The resulting atomic models of $CreS_{sat}$ and NB13 allowed for interpretation of $CreS_{wt}$ maps,
159 determined at lower resolutions (4.36 Å -5.78 Å) (**Fig. S4, Table S3**).

160 **Architecture of CreS filaments**

161 In the presence of MB13, $CreS_{wt}$ and $CreS_{sat}$ similarly assemble into a "supertwist"-like filament,
162 where two intertwined strands, I and II, are related by a two-fold axis perpendicular to the filament
163 axis (**Fig. 2B-C**). When looking at the map down this two-fold axis, each strand consists of four
164 partial CreS dimers (dimers A, B, C, and D for strand I, and symmetry related dimers A', B', C' and
165 D' for strand II) within a viewing window of ~960 Å wide. Each dimer is a parallel, polar coiled coil
166 of CreS molecules. Strands I and II are held together via interactions between CreS dimers. Taking
167 strand I as an example, inter-dimer interactions are found between a pair of dimers near their N-
168 termini (A-C pair) or their C-termini (B-D pair) in the longitudinal direction (i.e., along the filament
169 axis) (**Fig. 2D**). Hence, the two-stranded CreS filament presented here lacks polarity, as is the
170 case for the individual strands on their own. This is reminiscent of eukaryotic intermediate filaments
171 (IFs), which are also known to be non-polar [20-23]. Furthermore, each pair of longitudinally
172 associated dimers are structurally similar to each other, especially at the regions close to the inter-
173 dimer interface near the N-termini or C-termini. Thus, every pair of longitudinally associated dimers
174 are related by a local pseudo two-fold axis perpendicular to the inter-strand two-fold axis mentioned
175 above (**Fig. 2D**). Each pair of laterally interacting dimers (A-B pair or C-D pair) alternate at a
176 crossover due to them twisting around each other, giving rise to a crossover distance of ~480 Å
177 along the strand (**Fig. 2D**).

178 Assembling a nearly complete CreS dimer (residues 31-446 for $CreS_{sat}$ or 31-443 for $CreS_{wt}$),
179 based on the observed partial dimers A and B, resulted in an expanded atomic model of the strand
180 (**Fig. 2E**). The partial dimer C is superimposable with the equivalent part of the expanded dimer B
181 upon a shift of 564 Å and a rotation of 78° (**Fig. 2F**). Likewise, the partial dimer D is superimposable
182 with the equivalent region of the expanded dimer A upon a shift of 559 Å and a rotation of 53° (**Fig.**
183 **2G**). These observations indicate that every strand has a regular spacing of ~560 Å, which
184 corresponds to the length of a CreS molecule in a coiled coil. As a result, these transformations
185 enable each strand and the two-stranded filament to propagate in a roughly linear fashion.

186 **Assembly of CreS filaments**

187 A detailed structural analysis revealed five different types of dimer-dimer interactions that result in
188 the observed CreS filament (**Fig. 3A**). Within each strand, there are both lateral and longitudinal
189 interactions between CreS dimers. Types 1 and 2 involve longitudinal inter-dimer interactions near
190 the C-termini (pairs B-D and B'-D', residues ~443-457, most of which are disordered in our cryo-
191 EM maps) and near the N-termini (pairs A-C and A'-C', residues ~31-83), respectively (**Fig. 3B**).

192 Type 3 represents lateral inter-dimer interactions (pairs A-B, C-D, A'-B', C'-D') (**Fig. 3B**). Dimer-
193 dimer interactions between the two strands are primarily along the lateral direction, including type
194 4 (pair B-B', antiparallel) and type 5 (pairs B-D' and B'-D, parallel) (**Fig. 3B**). Whereas relatively
195 short stretches of amino acids are responsible for longitudinal interaction types, all lateral
196 interaction types cover long inter-dimer binding interfaces.

197 As mentioned in the **Introduction**, the central rod domains of eukaryotic IF proteins are generally
198 ~308 amino acids long, with the exceptions of nuclear lamins and invertebrate IF proteins (which
199 are ~350 amino acids long). It has been proposed to be divided into three coiled coil segments
200 with conserved lengths, 1A, 1B, and 2 [12], which are inter-connected by short linkers L1 and L12
201 (**Fig. S5A**). In contrast, CreS possesses a longer coiled coil rod domain (~364 amino acids), which
202 does not show equivalent linkers that disrupt the overall α-helical structure, based on our cryo-EM
203 maps (**Fig. S5A**). Both N-terminal and C-terminal segments of CreS are relatively short and do not
204 contain complex domains as seen in many eukaryotic IF proteins [24]. Furthermore, structural
205 comparisons of CreS filamentous assemblies with those of eukaryotic IF proteins are hindered by
206 a lack of atomic-level structural information concerning the assembly of eukaryotic IFs, despite
207 decades of research [21, 25-28]. Nevertheless, it has been established that the coiled coil dimer
208 of IF proteins functions as the basic subunit for IF assembly [12]. Four types of inter-dimer contacts,
209 A11, A12, A22, and ACN, have been proposed based on information gained primarily from X-ray
210 crystallographic studies of IF protein fragments and cross-linking mass spectrometry analyses of
211 IF protein oligomers [29-33] [20-23] [34]. These four contact types are shown in comparison to
212 those in CreS filaments in **Fig. S5B,** and their general lack of correspondence is elaborated on in
213 the **Discussion**. In particular, no counterparts of the ACN type (head-to-tail) are observed in our
214 *in vitro* CreS filament (**Fig. S5B)**. However, for eukaryotic IF proteins such as vimentin, it has been
215 proposed that four dimers laterally assemble into an octameric protofibril, of which multiple copies
216 come together in a symmetric way to produce the mature IF, which is often 10 nm wide [12, 26,
217 28, 35, 36]. The two-stranded CreS filament described here consists of four laterally associated
218 CreS dimers that arrange in an octameric manner very loosely reminiscent of that in the proposed
219 eukaryotic IF protofibril [26, 35] (**Fig. S5B, bottom**).

220 ***In vivo* crosslinking confirms crescentin filament architecture**

221 To address the *in vivo* relevance of the CreS filament structure determined *in vitro*, we probed
222 residue-residue contacts observed in the cryo-EM structure in *C. crescentus* cells using cysteine
223 cross-linking with a thiol-specific and cell permeable chemical cross-linker, bismaleimidoethane
224 (BMOE, spacer length ~8 Å). Guided by the CreS filament structure described above, we
225 introduced codons of pairs of cysteine residues into *creS*, which was expressed from a low-copy-
226 number plasmid under its native promoter in *C. crescentus* cells, in a *creS* deletion background
227 (**Materials and Methods)**. This yielded a protein level of CreS similar to the endogenous level in
228 wt strain CB15N (**Fig. S6A**). Cells expressing wt *creS* or a *creS* mutant this way had a cell

229 curvature comparable to wt strain, with two exceptions that will be discussed below (**Fig. S6B**).
230 We focused on residue pairs with a Cβ-Cβ distance of 6-12 Å at multiple inter-dimer interfaces in
231 both the $CreS_{sat}$ and $CreS_{wt}$ filament structures (**Table S4**).

232 For lateral dimer-dimer interactions (type 3, **Fig. 3**), we identified BMOE-dependent crosslinking
233 products for at least two residue pairs in each of three regions that are well separated along the
234 elongated inter-dimer interface (**Figs. 4 and 5**). In the absence of double-cysteine mutants, we
235 detected no signal or only weak background signal for wt CreS and single cysteine CreS mutants,
236 confirming that cross-linking was largely specific (**Fig. 4C**). The three lateral interaction regions
237 probed include "crossover" (A282C/D221C, K296C/A207C, and K296C/Q204C), "middle"
238 (T120C/R384C, A134C/K369C, and T131C/K369C), and "NC" (S34C/R419C and A37C/R419C),
239 where NC denotes interactions between the N-terminus and C-terminus proximal regions (**Figs. 4**
240 **and 5**).

241 For longitudinal interactions, we observed BMOE-dependent crosslinks between residue pairs
242 near the N-termini (E43C/S74C and E57C/E63C, region NN, type 2) and C-termini (M443C, region
243 CC, type 1), respectively (**Fig. 5**). Since all these inter-dimer interaction regions are most likely
244 important for the assembly of individual strands, these results indicate that the single-stranded
245 architecture observed *in vitro* likely acts as a structural unit for producing CreS assemblies *in vivo*.

246 **Subcellular organization of CreS filaments**

247 The ultrastructure of endogenous CreS assemblies at normal levels in *C. crescentus* has
248 previously been challenging to visualize [5-8, 37, 38]. We therefore imaged wt *C. crescentus* cells
249 where wt *creS* was moderately overexpressed using electron cryotomography (cryo-ET).
250 Tomographic reconstructions of these cells revealed an ~4 nm thick and on average 30-40 nm
251 wide (minimum ~15 nm, maximum ~60 nm wide) structure that lines the inner cell membrane at a
252 distance of ~ 5 nm and that spans a major portion of the cell's length on the concave side of the
253 cell (**Fig. 6A**). Consistent with this structure being CreS or CreS-containing filaments, over-
254 production of $creS_{\Delta N27}$, where the first 27 amino acids were truncated, in a *creS* deletion
255 background led to prominent bundles that detach from the inner cell membrane (**Fig. 6B**). This N-
256 terminal region is positively charged and had previously been shown to be required for attachment
257 of CreS to the inner cell membrane [6, 38]. Additionally, similar filamentous densities were not
258 detected in cryo-ET reconstructions of Δ*creS* cells (**Fig. 6C**). Furthermore, CTP synthase (CtpS)
259 is another filament-forming protein that localizes to the inner cell curvature in *C. crescentus* [39].
260 CtpS is known to interact with CreS and acts as a regulator of cell curvature [39]. Over-production
261 of wt *creS* in *ΔcreS* cells where *ctpS* expression was suppressed showed a similarly extended
262 structure lining the inner cell curvature (**Fig. 6D**). Thus, CreS can form filamentous structures along
263 the inner cell curvature in *Caulobacter* cells. This is in agreement with the subcellular localization
264 and low-resolution views of CreS as revealed by diffraction-limited fluorescence microscopy [5-7].

265

266 **Functional requirements**

267 Having determined the assembly and subcellular organization of CreS, we next addressed the
268 molecular determinants of CreS-dependent cell curvature generation. Ectopic expression of wt
269 *creS* in a heterologous system, *E. coli* strain C41, produced curved cells that are normally straight,
270 as evidenced by phase contrast light microscopy and cryo-EM (**Fig. S7A, E, I and L**) [6].
271 Consistent with a role of N-terminal and C-terminal segments in CreS filament assembly, purified
272 $CreS_{rod}$ that contains only the rod domain failed to assemble into long filaments *in vitro*, and
273 overexpression of $creS_{rod}$ did not curve *E. coli* cells (**Fig. S7B, F, J and L**). Further supporting this
274 idea is that two double-cysteine mutations, E43C/S74C and E57C/E63C, in the aforementioned
275 NN region (longitudinal inter-dimer interaction type 2) caused cell straightening in *C. crescentus*
276 (**Fig. S6B**). Moreover, previous mutational analyses showed that deleting each of four important
277 regions for CreS assembly observed in our structure resulted in altered assembly properties as
278 well as partial or nearly complete loss of cell curvature in *C. crescentus* [9]. These include the rod
279 domain (inter-dimer interaction types 3, 4, 5), the NN region (type 2), residues 121-143 (intended
280 to correspond to the L1 linker region in eukaryotic IF proteins, types 3 and 5), and the C-terminal
281 segment (type 1).

282 Nevertheless, correct CreS assembly is not the only functional requirement. Similar to previous
283 findings using *C. crescentus* [6], deleting the first 27 amino acids, which are disordered in our cryo-
284 EM maps, or mutating all negatively charged arginine residues to alanine residues in this region
285 (N27RtoA) yielded straight *E. coli* cells without disrupting CreS filament assembly *in vitro* (**Fig.**
286 **S7C, D, G, H, K, and L**). Thus, the faithful assembly and subcellular organization of CreS on the
287 inner membrane are both indispensable for its function in bacterial cell shape determination.

288 **DISCUSSION**

289 We have determined the complete structure of crescentin and its filament (**Figs. 1-3**). To our
290 knowledge, this has so far not been achieved for any other IF or IF-like protein [11, 27]. Coiled
291 coil-containing filaments are often refractory to structure determination by X-ray crystallography
292 and also cryo-EM because of their elongated nature, the smoothness of the filaments, and
293 heterogeneity of the filaments formed. AlphaFold 2 predictions on coiled coil proteins are not as
294 powerful as for globular proteins [18], which is also the case for crescentin (**Fig. S1C**). To
295 circumvent these problems, we obtained a crescentin-binding nanobody that we converted into a
296 megabody for cryo-EM structural studies. Because the megabody bound close to the C-terminus
297 of crescentin and all N- and C-terminal ends in the crescentin filament are located in close
298 proximity, this enabled us to obtain a reliable structure of that part at close to 3.3 Å resolution.
299 Further along the filament, atomic modelling was less certain, but the maps indicated that the rod
300 domain of crescentin most likely forms a continuous coiled coil, without flexible linkers. Because
301 we worried about the effect of the conditions used to obtain the filaments, including the use of the
302 megabody, we used site-directed *in vivo* cysteine crosslinking to verify the obtained structure
303 (**Figs. 4-5**). Given that we could not find any major discrepancies, we are confident that the
304 obtained structure is a good representation of the structures crescentin forms in cells. Further
305 supporting this notion is that mutations in a number of structurally important regions for CreS
306 assembly identified here lead to an impaired or abolished cellular function of CreS, based on our
307 and previous results (**Fig. S7**) [9].

308 Cryo-ET of cells overexpressing crescentin revealed filamentous structures on the concave sides
309 of cells, close to the inner membrane (**Fig. 6**). Because of earlier misunderstandings [39], we
310 demonstrated that the observed structures are not CTP synthase (CtpS). From these findings the
311 question arises how the slowly twisting *in vitro* filaments correspond to the band-like appearance
312 of crescentin in cells. While it is difficult to answer this without further and higher-resolution insights
313 into the structure of the *in vivo* crescentin assemblies, it is important to note that it has been
314 reported that when crescentin filamentous structures are released from the membrane through the
315 inhibition of MreB or cell wall synthesis, the filaments form helical structures [6]. It seems plausible
316 that membrane attachment removes some of the twisting that our *in vitro* structure revealed. The
317 cryo-ET data shows crescentin to be close to the membrane (~5 nm in distance). We propose that
318 this distance could slow down or even stop elongasomes moving past as they circle the cells along
319 their short axes to make cell wall [40-42].

320 We confirmed earlier results that the first 27 residues of crescentin are required for its membrane
321 localization [6] (**Fig. 6**). Despite trying, we have been unable to demonstrate convincingly direct
322 membrane binding of crescentin filaments to lipid membranes or liposomes *in vitro*. Given the
323 above mentioned finding that the inhibition of cell wall synthesis or MreB removes crescentin from
324 the membrane [6], it seems likely that membrane attachment, involving the first 27 residues of

325 crescentin, is mediated by another cellular component. One such component could be MreB [7],
326 although AlphaFold 2 is not able to predict a complex between crescentin and MreB in our hands.
327 Possibly also speaking against this idea is the finding that crescentin over-expression in *E. coli*
328 leads to curved cells [6]. If another component is needed to localize crescentin to the membrane,
329 then it must be present (and functional) in *E. coli* as well.

330 Our structure of crescentin and its filament enables us to compare it to what is known about
331 eukaryotic IF proteins and their filaments. It is important to point out again that there is currently
332 no complete atomic structure of any IF protein and in particular of an IF filament [11, 26]. Given
333 the formidable technical difficulties with these proteins, considerable efforts have been spent using
334 a "divide and conquer" approach combining X-ray crystallography and crosslinking, to obtain
335 pseudo-atomic models of IF proteins and filaments. Comparing our structure with these models
336 reveals several important similarities and differences (**Fig. 3, Fig. S5**). Crescentin and most IFs
337 form long parallel coiled coil dimers with disordered domains at each end. Vimentin and other
338 cytoplasmic IFs have been shown to form tetramers, two dimers coming together via their coil1
339 domains (A11 contact) [20-23]. No such contact exists in the structure of the crescentin filament.
340 In fact, apart from IF's A12 contact there does not seem to be much similarity in the way dimers
341 pack into larger fibres between IFs and crescentin. Furthermore, the most important difference
342 between them is the longitudinal contacts. In crescentin, they are exclusively N-N (head-to-head)
343 and C-C (tail-to-tail), whereas all the current IF models assume ACN contacts that link dimers
344 head-to-tail. It is, however, important to point out that the experimental evidence for ACN contacts
345 is sparse. Their existence seems to be derived from nuclear lamins that form chains of head-to-
346 tail dimers instead of tetramers [34] and from the fact that it is difficult to build larger IF filament
347 models from A11 tetramers without ACN head-to-tail arrangements.

348 All IF proteins contain a stutter that inserts into the coiled coil-forming heptad repeat four extra
349 residues. This is thought to not interrupt the coiled coil *per se*, but to change the superhelical
350 arrangement such that the two helices run more parallel for a short distance. Crescentin also
351 contains a stutter (residues 406-409) and we have investigated the consequences of removing it
352 by reverting the repeat pattern back to regular heptad repeats by inserting three residues, Ser, Ala
353 and Thr (SAT), before position 406 [9]. While it has been reported that such a modification
354 abolishes crescentin's ability to curve cells [9], we have found little evidence that it changes its
355 behaviour *in vitro*. The structures of the WT and SAT versions are very similar, except that the
356 SAT version is slightly longer because the helices contain one almost complete extra helical turn.
357 It will need further work to investigate this in more detail. For example, the stutter might be needed
358 to form higher-order assemblies such as the ones seen in cells (**Fig. 6**).

359 Going forward it will be important to figure out if crescentin filaments locally modify and reduce cell
360 wall synthesis via the elongasome as proposed and how crescentin filaments localize to the inner
361 membrane since we could not reconstitute membrane binding *in vitro*. Because crescentin

filaments are thin and smooth, cellular tomography is unlikely to deliver directly how this is done. Genetic and *in vitro* approaches will have to be pushed further to provide answers.

There are a number of other IF-like proteins known in bacteria, such as Scy and Filp in Streptomyces [43]. Beyond these, other bacterial coiled coil rich proteins (CCRPs), whose evolutionary relationships to IFs are even more enigmatic, such as CrvA and CrvB in *V. cholerae* and CcfM in *M. gryphiswaldense,* share a similar cellular function with CreS in maintaining curved bacterial cell shapes [44, 45]. It will be important to investigate what structures these proteins form. Revealing the evolutionary relationships between IF and their bacterial counterparts will also require more certainty about the structures of IF filaments, an area of eukaryotic structural cell biology that needs urgent attention, perhaps using similar nanobody and cryo-EM approaches as pioneered here. But even with the dissimilarities unearthed, between the crescentin filament structure and the current model of IF filaments, it is intriguing that non-polar octameric filaments made out of long parallel coiled coil dimers characterize both sets of proteins. A picture emerges in which long, extended parallel coiled coil proteins have evolved to produce a variety of filament architectures to generate mechanical and polymerization properties that are required for a multitude of cellular functions, across the tree of life.

379 **MATERIALS AND METHODS**

380 ***Caulobacter crescentus* and *Escherichia coli* strains.** *C. crescentus* cells were grown in
381 peptone yeast extract (PYE) media at 30°C [46]. Antibiotics were used when required in liquid
382 (solid) media at the following concentrations: 1 (1) µg/mL and 1 (2) µg/mL for chloramphenicol and
383 oxytetracycline, respectively. For ectopic expression of wildtype (wt) *creS* and its variants in *C.*
384 *crescentus*, a parental strain as indicated was transformed with an appropriate plasmid, based on
385 either the low-copy-number pCT133 or medium-copy-number pCT155 vector (**Table S1**). To
386 generate these plasmids, the sequences of *creS* and their native promoter were amplified from
387 strain CB15N and then assembled into the pCT133 or pCT155 backbone using Gibson assembly
388 (New England Biolabs). For protein expression in *E. coli*, an appropriate expression plasmid (**Table**
389 **S1**) was electroporated into C41 (DE3) cells unless stated otherwise. Ampicillin and kanamycin
390 were used at 100 µg/mL and 50 µg/mL, respectively, when required. *E. coli* growth and induction
391 were both at 37°C unless stated otherwise.

392 For imaging, *C. crescentus* strains were grown overnight in PYE medium with the appropriate
393 antibiotics, sub-cultured, and grown to mid-log phase. Glucose was used at a concentration of
394 0.2 % (w/v) to suppress protein expression driven by the leaky, xylose-inducible promoter. *E. coli*
395 strains over-expressing CreS constructs were grown overnight in Luria-Bertani (LB) media with
396 ampicillin to stationary phase, sub-cultured, grown to $OD_{600\ nm}$ ~0.2, and induced by 0.05 mM
397 IPTG for ~2.5 h.

398 **Crescentin expression and production.** The amino acid sequences of the proteins used in this
399 study are listed in **Table S2**. Non-tagged wt crescentin ($CreS_{wt}$, GenBank accession identifier:
400 ACL97278.1) was produced in *E. coli* BL21 (DE3) cells carrying a pET29a-based plasmid for
401 $CreS_{wt}$ expression (strain CJW1659, C. Jacobs-Wagner, Stanford University, USA) [9]. To produce
402 a "stutter mutant", $CreS_{sat}$, that has a three amino acid insertion (Ser, Ala and Thr, SAT) before
403 residue 406 to remove the stutter, strain CJW2045 (C. Jacobs-Wagner) was used [9]. Other non-
404 tagged CreS constructs included $CreS_{rod}$ (amino acids 80-444), $CreS_{\Delta N27}$ (amino acids 28-457),
405 and $CreS_{N274RtoA}$ (all Arg mutated to Ala in amino acids 1-27). These were constructed using
406 Gibson assembly (New England Biolabs) and employing pFE127 as a parental plasmid, which is
407 a pHis17-based plasmid for expressing CreS-His, full length CreS followed by GSHHHHHH. The
408 expression and purification of all non-tagged CreS proteins followed the same procedures below.
409 All purification steps were carried out at 4°C. *E. coli* cells were grown in 2×TY media with
410 kanamycin or ampicillin to reach an $OD_{600\ nm}$ of ~0.6 before 1 mM IPTG was added to induce
411 protein expression for 4 h. Cells were then spun down, and pellets were lysed by sonication in 50
412 mM sodium phosphate buffer, 150 mM NaCl, pH 7.2, 0.1% (v/v) Triton X-100, supplemented with
413 lysozyme, DNase, RNase, and protease inhibitor cocktail (Roche). After centrifugation at 45,000
414 ×g for 40 min, the supernatant was incubated with 30 g/L of Avicel PH-10 cellulose microspheres
415 (Sigma-Aldrich) overnight [47]. The microspheres were washed with 50 mM sodium phosphate

416 buffer, 1 M NaCl, pH 7.2, followed by elution with 50 mM sodium phosphate buffer pH 7.2, 150
417 mM NaCl, 40% (w/v) glucose. The eluate was dialyzed against 50 mM CHES, pH 10, and
418 concentrated before being injected onto a HiLoad 16/600 Superdex 200 PG column (Cytiva) for
419 gel filtration in 5 mM Tris-HCl, pH 8. Peak fractions corresponding to CreS were pooled and
420 concentrated using an Amicron Ultra-15 centrifugal filter (30 kDa molecular weight cutoff [MWCO],
421 Millipore) to a final concentration of ~9 g/L.

422 To purify CreS-His, cells were lysed by sonication in 50 mM Tris-HCl, 300 mM NaCl, 2 mM tris(2-
423 carboxyethyl)phosphine (TCEP), pH 8 (buffer A), supplemented with lysozyme, DNase, RNase,
424 and protease inhibitor cocktail (Roche). The lysate was cleared by centrifugation at 75,000 ×g for
425 1 h and filtered before being loaded onto a 5 mL HisTrap HP column (Cytiva). After washing with
426 increased concentrations (0, 20, 50, and 80 mM) of imidazole in buffer A in a stepwise manner,
427 proteins were eluted with 500 mM imidazole in buffer A. Upon concentration, the eluate was further
428 purified via size exclusion chromatography as above, and protein fractions were treated in the
429 same way as mentioned above.

430 **Expression and production of NB13 and MB13.** Camelid nanobodies (NBs) were raised and
431 selected against purified $CreS_{wt}$ (in 5 mM Tris-HCl, pH 8) through the commercial service provided
432 by the VIB Nanobody Core, Vrije Universiteit Brussel, Belgium. Twenty five of 97 NB clones
433 delivered were chosen based on their sequence diversity and antigen binding capacity for another
434 round of selection against CreS filaments at both pH 7 and pH 6.5, using an enzyme-linked
435 immunosorbent assay (ELISA). To identify suitable NB clones for biochemical and structural
436 studies, purified NB and megabodies (MB, a large nanobody derivative described below [13]) were
437 produced for each of the top eight clones selected based on the ELISA data. The binding properties
438 of each protein to purified CreS were examined using size exclusion chromatography (pH 8) and
439 negative staining electron microscopy (pH 7 and pH 6.5). The final selection was clone No. 13,
440 whose megabody, MB13, together with CreS, forms a stable complex at pH 8 that assembles into
441 single, uniform filaments *in vitro* upon acidification.

442 To produce the nanobody version of clone No. 13, namely NB13, the non-suppressor *E. coli* strain
443 WK6 [48] was transformed with a phagemid vector pMECS containing the PelB leader sequence,
444 followed by the NB13 sequence and followed by an HA tag and a 6×His tag. For periplasmic
445 expression of the megabody of NB13, MB13, with a C-terminal 6×His tag, a pET-22b-based
446 plasmid was generated using Gibson assembly (New England Biolabs). In this construct, NB13
447 was grafted onto a circular permutant of the scaffold protein YgjK (*E coli* K12 glucosidase, 86 kDa)
448 as previously described [13]. The resultant plasmid was electroporated into C41 (DE3) cells. For
449 both NB13 and MB13, cells were grown in Terrific Broth with ampicillin, 2 mM $MgCl_2$ and 0.1%
450 (w/v) glucose until $OD_{600\ nm}$ ~0.6. Protein expression was induced at 25°C for ~19 h with 1 mM
451 IPTG. All purification steps were carried out at 4°C unless stated otherwise. Cell pellets were
452 treated with 0.2 M Tris pH 8, 0.5 mM EDTA, 0.5 M sucrose (TES) on ice for 1 h, and four times

453 diluted TES on ice for another 1.5 h. After clearance by centrifugation at 50,000 ×g for 30 min, the
454 resultant periplasmic extract was loaded onto a 5 mL HisTrap HP column (Cytiva). The column
455 was washed sequentially with a) 20 mM Tris pH 8, 900 mM NaCl, b) 20 mM imidazole in buffer B
456 (20 mM Tris-HCl, 50 mM NaCl, pH 8), c) 50 mM imidazole in buffer B, and eluted with 500 mM
457 imidazole in buffer B. For NB13, the eluate was sufficiently pure and concentrated using an
458 Amicron Ultra-15 centrifugal filter (3 kDa MWCO, Millipore) to a final concentration of ~14 g/L. For
459 MB13, the eluate was concentrated, and further purified via gel filtration using a Superdex 200
460 Increase 10/300 GL column (Cytiva), equilibrated in 10 mM Tris-HCl, 20 mM NaCl, pH 8. Fractions
461 corresponding to MB13 were pooled and concentrated using a Vivaspin Turbo 15 centrifugal filter
462 (50 kDa MWCO) to a final concentration of ~36 g/L. Purified proteins were flash frozen in liquid
463 nitrogen and stored at -80°C.

464 **Electron microscopy of negatively stained samples.** Purified CreS proteins were diluted into
465 25 mM PIPES, pH 6.5 to reach a concentration of ~0.2 g/L, and incubated at room temperature
466 (RT) for 15 min to allow polymerization. The resultant sample was applied onto 400-mesh
467 continuous carbon film copper grids (Electron Microscopy Sciences), which were then stained with
468 2% (w/v) uranyl acetate. Grids were imaged using a Tecnai 12 electron microscope (Thermo Fisher
469 Scientific, TFS) equipped with an Orius CCD camera and operated at 120 kV.

470 **Single particle cryo-EM sample preparation.** Purified $CreS_{wt}$ or $CreS_{sat}$ were incubated with
471 MB13 at a molar ratio of 1:4 in 5 mM Tris-HCl pH 8 at 4°C overnight. The resultant mixture was
472 applied onto a Superose 6 Increase 3.2/300 gel filtration column (Cytiva) in 5 mM Tris-HCl pH 8.
473 Fractions B9 to B5, corresponding to the CreS-MB13 complex (**Fig. 1, Fig. S1**), were pooled and
474 concentrated using a Vivaspin 500 centrifugal filter (100 kDa MWCO). The sample was diluted into
475 25 mM PIPES pH 6.5 to allow for polymerization at RT for 15 min, and then treated with CHAPS
476 through the addition of a 1% (w/v) CHAPS stock solution to reach a final concentration of 0.05%
477 (w/v) at RT for 5 min. This procedure consistently yielded uniform, single CreS filaments in complex
478 with MB13.

479 For cryo-EM grid preparation, sample aliquots of 3 µL were applied onto UltrAuFoil R2/2 grids (300
480 mesh, Quantifoil). Grids were blotted for 1 s at 10°C with 100% relative humidity and immediately
481 plunge frozen into liquid ethane using a Vitrobot Mark IV system (TFS). Movies of MB13-decorated
482 CreS filaments embedded in vitreous ice were collected at liquid nitrogen temperature using a
483 Titan Krios transmission electron microscope, operated at 300 kV and using the programme EPU
484 (TFS). For dataset $CreS_{sat}$, movies were collected at a nominal magnification of 81,000× in super
485 resolution mode using a K3 direct electron detector (Gatan), resulting in a super resolution pixel
486 size of 0.53 Å/pixel on the specimen level. The total exposure was 53 $e^-/Å^2$ in 2.4 s with a dose
487 rate of 25 e^-/pixel/s, a frame rate of 60 ms, and a defocus range of 0.4-2.6 µm. For dataset $Cres_{wt}$,
488 movies were collected at a nominal magnification of 75,000× using a Falcon 4 camera (TFS),
489 giving a physical pixel size of 1.08 Å/pixel on the specimen level. The total exposure was 34 $e^-/Å^2$

490 in 10 s with a dose rate of 4 e^-/pixel/s, a frame rate of 4 ms (EER - electron event representation),
491 and a defocus range of 0.4-4.0 μm. Data collection statistics have been summarized in **Table S3**.

492 **Image processing.** The image processing procedures for datasets $CreS_{wt}$ and $CreS_{sat}$ were
493 essentially the same except for slight differences in pixel size and box size (see **Table S3** for
494 details). The following description focuses on dataset $CreS_{sat}$. Movies were corrected for inter-
495 frame motions using MotionCor2 [49]. Aligned frames were summed and down-sampled to
496 produce individual micrographs (1.06 Å/pixel) that were used for estimation of contrast transfer
497 function (CTF) parameters using CTFFIND4 [50]. Nearly every single filament on the micrographs
498 (e.g., **Fig. 1B**) showed a regular spacing of ~60 nm between neighbouring "nodes", of which each
499 represents a segment of the CreS filament decorated with MB13 molecules. About 870,000
500 particles centred on individual nodes were picked from all micrographs that had been denoised for
501 picking purposes using a neural network model pre-trained in Topaz [51, 52].

502 The following steps involved the alternate use of Relion 3.1 [53] and cryoSPARC [54]. Particles
503 were first extracted with a box size of 100 pixels and 4.24 Å pixel size (Fourier cropping throughout
504 the processing). About 690,000 particles were retained after reference-free 2D classification where
505 low-quality particles were identified and removed. Six *ab initio* 3D references were then generated,
506 and the best resolved reconstruction was used as a starting reference for global particle alignments.
507 Particles were subsequently re-extracted with a box size of 200 pixels and 2.12 Å pixel size.
508 Heterogenous refinement in 3D with four classes resulted in one class of particles that showed
509 partial occupancy of MB13 molecules and those were discarded. Visual inspection of the map
510 reconstructed using the remaining ~600,000 particles suggested the presence of a two-fold
511 symmetry axis perpendicular to the filament axis. Thus, the poses of these particles were then
512 refined where C2 symmetry was imposed. Next, to produce high resolution reconstructions,
513 particles were re-centred and re-extracted with 1.325 Å pixel size and with a box size of 320 pixels,
514 hereafter referred to as "small box" (SB). In parallel, given that a box size of 400 Å is not sufficient
515 to reveal the structure of a complete CreS molecule, another set of particle images were extracted
516 with 1.59 Å pixel size and a box size of 600 pixels, hereafter referred to as "large box" (LB). The
517 following procedures were applied independently to both sets of particle images. After 3D
518 refinement and Bayesian polishing [55], the densities of scaffold proteins (i.e., YgjK) were
519 subtracted from original particle images. The resultant particle images, which essentially represent
520 nanobody-bound CreS filament segments were subjected to local refinement with C2 symmetry,
521 yielding the reconstruction SAT-SB-C2 for set SB (SAT-LB-C2 for set LB, see **Table S3**). To
522 improve map resolutions, particles were expanded by the C2 symmetry [56], and the densities
523 corresponding to one of two symmetry-related copies were subtracted from images. Subsequent
524 local refinement with C1 symmetry led to a higher resolution reconstruction, SAT-SB-C1 for set
525 SB (SAT-LB-C1 for set LB). The resolutions of reconstructions were estimated based on two
526 methods. One was the Fourier Shell Correlation (FSC) between two independently calculated half
527 maps (Gold Standard FSC) using an FSC cut-off of 0.143 [57]. The other was a model-map FSC

528 between the final EM map and a map computed based on an atomic model (described below),
529 built into and refined against the EM map, using an FSC cut-off of 0.5 [58]. All maps were
530 sharpened using a deep learning-based programme, DeepEMhancer [59]. Local resolution was
531 assessed using Relion [53].

532 **Atomic model building and refinement.** The reconstructions SAT-SB-C1 and SAT-LB-C1
533 showed a structure consisting of four partial CreS coiled coil dimers (i.e., two pairs of longitudinally
534 or laterally associated partial dimers) (**Fig. 2**). The two partial dimers within each longitudinal pair
535 are related by pseudo two-fold symmetry and are held together by interactions between the C-
536 termini or between the N-termini. Thus, each lateral pair is formed by two segments, the N- and C-
537 segments, with their N-terminus and C-terminus oriented towards the pseudo two-fold symmetry
538 axis, respectively. For each segment, we computationally determined the amino acid register by
539 aligning the observed map density with the amino acid sequence of $CreS_{sat}$ using a previously
540 described approach [60]. In this process, we focused on a fragment of ~20 amino acids that
541 showed the most prominent side chain densities in SAT-SB-C1. Briefly, every amino acid position
542 in the fragment was assigned a number among 0-6 based on the estimated size of the side chain
543 density by visual inspection. The resultant sequence of numbers was searched against that of the
544 entire amino acid sequence of $CreS_{sat,}$ according to a scoring matrix, where a mismatch of a small
545 residue in the sequence with the observed large side chain density at a given position was
546 penalized. The amino acid register determined *in silico* this way was further supported by several
547 lines of evidence. First, the resultant amino acid sequence fitted well into the observed side chain
548 density (e.g., **Fig. S3**), as judged by visual inspection. Second, the binding region of NB13 on CreS
549 was mapped to residues 413-433 (**Fig. 2A**), consistent with the assigned amino acid register for
550 the C segment. Third, whole cell cysteine crosslinking revealed residue-residue contacts that were
551 consistent with the atomic model of the single-stranded structure (**Figs. 4-5**). In particular, laterally
552 associated inter-dimer residue-residue contacts supported the assigned amino acid register for the
553 N segment (**Fig. 4**).

554 To interpret the highest resolution reconstruction SAT-SB-C1, we predicted the coiled coil dimeric
555 structures for the N segment and C segment based on their estimated length using CCFold [61].
556 A homology model of NB13 was generated using SWISS-MODEL [62] with the structure of a
557 nanobody (NB-ALFA) against the ALFA-tag (PDB entry 6I2G) as a template. These starting atomic
558 models were fitted into the cryo-EM map in Chimera [63], followed by manual model re-building in
559 Coot [64]. In this process, the orientation of NB13 was initially determined based on the β-strands
560 identified in the map and was similar to that of NB-ALFA when complexed with the ALFA-tag that
561 forms an α-helix. The atomic coordinates were subsequently refined against the map in real space
562 using Phenix [65, 66], where secondary structure restraints were applied. Multiple cycles of manual
563 model rebuilding and real space refinement improved the fitting of the model into the density map
564 and model geometry. To interpret the reconstruction SAT-LB-C1, we expanded the atomic model
565 for SAT-SB-C1 by fitting predicted structures of the remaining regions of $CreS_{sat}$. In local regions

566 where the map resolution was not sufficient for an unambiguous secondary structural assignment
567 between a helix and a loop, we assumed that it was helical according to coiled coil and secondary
568 structure predictions. The expanded atomic model was rebuilt and refined using the same
569 procedures described above. For each of the C2 reconstructions, SAT-SB-C2 and SAT-LB-C2,
570 the atomic model for their C1 counterpart and the C2 symmetry related copy were fitted separately
571 into the map as rigid bodies, and then combined into a single atomic model. Per-atom real space
572 refinement of the resultant atomic model was not performed due to the low-resolution nature of
573 these reconstructions compared with their respective C1 counterparts.

574 The omission of three-amino acids (SAT) in $CreS_{wt}$ with respect to $CreS_{sat}$ produces a stutter that
575 locally disrupts the continuity of the dimeric heptad-repeat coiled coil [67]. Thus, it is reasonable to
576 assume that the preceding and later segments along the coiled coil have little structural changes
577 upon introduction of the stutter. In line with this, we found that the overall arrangement of $CreS_{wt}$
578 dimers in the filament is similar to that observed for $CreS_{sat}$ (**Fig. 2**). We determined the amino acid
579 register for the C segment using NB13 molecules as a spatial reference and for the N segment by
580 assuming that $CreS_{wt}$ and $CreS_{sat}$ share the same lateral, inter-dimer interactions between the N-
581 proximal region and C-proximal region. To interpret the reconstruction WT-SB-C1, we used the
582 $CreS_{sat}$ structure as a starting atomic model and replaced the segment corresponding to the stutter
583 region in $CreS_{wt}$ with a sequence adjusted, stutter-containing fragment in vimentin (PDB entry
584 1GK4). The resultant atomic model was subjected to multiple rounds of model rebuilding and real
585 space refinement against the map, as mentioned above. For the reconstruction WT-LB-C1, the
586 atomic model for WT-SB-C1 was expanded with appropriate segments from the $CreS_{sat}$ structure,
587 followed by model rebuilding and refinement. The atomic model for each of the two C2
588 reconstructions, WT-SB-C2 and WT-LB-C2, was generated using the aforementioned rigid body
589 fitting approach.

590 The final atomic models were geometrically validated based on the criteria of MolProbity [68].
591 Model statistics have been summarized in **Table S3**. All figures were generated using Pymol
592 (https://pymol.org/) or Chimera [63].

593 **Electron cryotomography (cryo-ET).** *C. crescentus* cells were pelleted at 8,000 ×g for 2 min and
594 resuspended in PYE media to reach an $OD_{600\ nm}$ of ~5. The resuspension was mixed with protein
595 A-conjugated 10 nm gold fiducials (BBI Solutions). Aliquots of 2.5 µL sample were applied onto
596 freshly glow-discharged Quantifoil R 3.5/1 Cu/Rh (200 mesh) grids, followed by blotting for 2-3 s
597 and plunge freezing into liquid ethane using a Vitrobot Mark IV system (TFS). Specimens were
598 imaged using a Titan Krios transmission electron microscope (TFS), operated at 300 kV and
599 equipped with a BioQuantum imaging filter (Gatan) and a K3 camera (Gatan). Tilt series were
600 collected from -60° to 60° in 2° increments at a nominal magnification of 19,500× with a pixel size
601 of 3.84 Å /pixel using SerialEM [69]. The total exposure was ~180 $e^-/Å^2$ with a defocus of 8-10 µm.

602 Tilt series were aligned automatically using Batchruntomo in IMOD [70, 71], and tomograms were
603 reconstructed using the SIRT algorithm in TOMO3D [72].

604 **Mapping of the NB13 binding site on crescentin.** To map the binding site of NB13 on CreS,
605 CreS-His variants were constructed for ectopic expression in C41 (DE3) cells by introducing either
606 a truncation or a substitution into the parental pFE127 plasmid via site-directed PCR-based
607 mutagenesis (KLD enzyme mix, New England Biolabs). Protein expression was induced for 4 h at
608 37°C by adding 1 mM IPTG when cell cultures reached $OD_{600\ nm}$ ~0.5 in LB with ampicillin. Cell
609 pellets were washed twice with cold PBS and lysed using CelLytic Express (Sigma-Aldrich) with
610 protease inhibitor cocktail (Roche) at RT for 20 min. Purified CreS controls and equivalent OD_{600}
611 $_{nm}$ units of cleared cell lysates by centrifugation were resolved on a 4-20% SDS-polyacrylamide
612 gel (Bio-Rad). In this step, each biological sample was split into two halves, and the two halves
613 were loaded separately on the same gel. For Western blotting analysis, one half was
614 immunoblotted with NB13 (7 μg/mL) followed by washing and probing with α-HA-peroxidase
615 (1:1000, Roche), whereas the other half was probed with α-His-peroxidase only (1:4000, TFS).

616 **Whole cell cysteine crosslinking.** *C. crescentus* strains harbouring a low-copy-number plasmid
617 for expressing CreS or its mutants were grown overnight in PYE with oxytetracycline, sub-cultured,
618 and grown to $OD_{600\ nm}$ 0.5-0.6. Control strains, CB15N and CB15N Δ*creS* were grown in the same
619 way without antibiotics. About 1.2 $OD_{600\ nm}$ units of cells were spun down at 8,000 ×g for 3 min,
620 and then kept on ice for the following steps. Pellets were washed with cold PBS and resuspended
621 in 80 μL of cold PBS, followed by a 10 min reaction upon addition of 2 μL DMSO or
622 bis(maleimido)ethane (BMOE, final concentration 0.5 mM, ~8 Å arm length, TFS) in DMSO. The
623 reaction was quenched by adding 1 μL of β-mercaptoethanol (BME, stock ~2.3 mM). Cells were
624 then lysed using CelLytic Express (Sigma-Aldrich), supplemented with protease inhibitor cocktail
625 (Roche) at RT for 15 min. The suspension was incubated at 70°C for 5 min in the presence of LDS
626 loading buffer supplemented with 4% (v/v) BME. Samples equivalent to 0.1 $OD_{600\ nm}$ units of cells
627 were resolved on a 4-20% SDS-polyacrylamide gel (Bio-Rad), and immunoblotted with purified
628 NB13 (16 μg/mL), followed by washing and then probing with α-HA-peroxidase (1:1000, Roche).

629 **Light microscopy** Cells grown in conditions described above were imaged upon immobilization
630 on 1% agarose pads. Images were acquired using a Nikon Eclipse Ti2 microscope equipped with
631 a Neo sCMOS camera (Andor) and a Nikon Plan APO DIC objective (100×, numerical aperture
632 1.40). Cell segmentation and cell curvature analysis were performed using MicrobeJ [73] as a
633 plugin in ImageJ [74]. The number of cells analysed was between 114 and 519 for *C. crescentus*
634 strains, and between 140 and 293 for *E. coli* strains. For each strain, mean cell curvature (μm^{-1})
635 and standard deviation (μm^{-1}) were computed and presented.

DATA AVAILABILITY: The atomic coordinates derived using reconstructions SAT-SB-C2, SAT-SB-C1, SAT-LB-C2, SAT-LB-C1, WT-SB-C2, WT-SB-C1, WT-LB-C2, and WT-LB-C1 have been deposited with the Protein Data Bank (accession numbers 8AFH, 8AFE, 8AJB, 8AHL, 8AFM, 8AFL, 8AIX, 8AIA). The cryo-EM maps of SAT-SB-C2, SAT-SB-C1, SAT-LB-C2, SAT-LB-C1, WT-SB-C2, WT-SB-C1, WT-LB-C2, and WT-LB-C1 have been deposited with the Electron Microscopy Data Bank (accession numbers EMD-15398, EMD-15395, EMD-15476, EMD-15446, EMD-15402, EMD-15401, EMD-15473, EMD-15465). Table S3 summarises details.

AUTHOR CONTRIBUTIONS: Y.L. and J.L. designed research; Y.L performed most research, F.v.d.E made CreS constructs; Y.L. and J.L. analysed data; Y.L. and J.L. wrote the manuscript.

DECLARATION OF CONFLICTS: The authors declare no conflict of interest.

ACKNOWLEDGEMENTS AND FUNDING SOURCES: We thank all members of the MRC Laboratory of Molecular Biology (Cambridge, LMB) electron microscopy facility for excellent EM support, all members of the LMB light microscopy facility for technical support, Diamond Light Source (Harwell, UK) for access to, and support at the cryo-EM facilities at the UK's National Electron Bio-imaging Centre (eBIC), funded by the Wellcome Trust, MRC and BBSRC, and Toby Darling and Jake Grimmett (LMB Scientific Computing) for support. We are grateful to Lucy Shapiro (Stanford University, USA), Christine Jacobs-Wagner (Stanford University, USA), Zemer Gitai (Princeton University, USA), and Michael Laub (MIT, USA) for sharing *C. crescentus* and *E. coli* strains and plasmids used in this work. We thank all members of the Löwe group for helpful discussions. This work was funded by the Medical Research Council, UK (U105184326 to J.L.) and the Wellcome Trust (202754/Z/16/Z to J.L.).

660 **REFERENCES**

661 1. Young KD (2006) The selective value of bacterial shape. *Microbiol Mol Biol Rev* 70(3):660-
662 703.
663 2. Surovtsev IV & Jacobs-Wagner C (2018) Subcellular Organization: A Critical Feature of
664 Bacterial Cell Replication. *Cell* 172(6):1271-1293.
665 3. Skerker JM & Laub MT (2004) Cell-cycle progression and the generation of asymmetry in
666 *Caulobacter crescentus*. *Nat Rev Microbiol* 2(4):325-337.
667 4. Persat A, Stone HA & Gitai Z (2014) The curved shape of *Caulobacter crescentus* enhances
668 surface colonization in flow. *Nat Commun* 5:3824.
669 5. Ausmees N, Kuhn JR & Jacobs-Wagner C (2003) The bacterial cytoskeleton: an intermediate
670 filament-like function in cell shape. *Cell* 115(6):705-713.
671 6. Cabeen MT, Charbon G, Vollmer W*, et al.* (2009) Bacterial cell curvature through mechanical
672 control of cell growth. *EMBO J* 28(9):1208-1219.
673 7. Charbon G, Cabeen MT & Jacobs-Wagner C (2009) Bacterial intermediate filaments: *in vivo*
674 assembly, organization, and dynamics of crescentin. *Genes Dev* 23(9):1131-1144.
675 8. Esue O, Rupprecht L, Sun SX, & Wirtz D (2010) Dynamics of the bacterial intermediate
676 filament crescentin *in vitro* and i*n vivo*. *PLoS One* 5(1):e8855.
677 9. Cabeen MT, Herrmann H & Jacobs-Wagner C (2011) The domain organization of the bacterial
678 intermediate filament-like protein crescentin is important for assembly and function.
679 *Cytoskeleton (Hoboken)* 68(4):205-219.
680 10. Herrmann H & Aebi U (2000) Intermediate filaments and their associates: multi-talented
681 structural elements specifying cytoarchitecture and cytodynamics. *Curr Opin Cell Biol*
682 12(1):79-90.
683 11. Vermeire PJ, Stalmans G, Lilina AV*, et al.* (2021) Molecular Interactions Driving Intermediate
684 Filament Assembly. *Cells* 10(9).
685 12. Herrmann H & Aebi U (2016) Intermediate Filaments: Structure and Assembly. *Cold Spring*
686 *Harb Perspect Biol* 8(11).
687 13. Uchanski T, Masiulis S, Fischer B*, et al.* (2021) Megabodies expand the nanobody toolkit for
688 protein structure determination by single-particle cryo-EM. *Nat Methods* 18(1):60-68.
689 14. Gilbert DS & Newby BJ (1975) Neurofilament disguise, destruction and discipline. *Nature*
690 256(5518):586-589.
691 15. Steinert PM, Idler WW & Zimmerman SB (1976) Self-assembly of bovine epidermal keratin
692 filaments *in vitro*. *J Mol Biol* 108(3):547-567.
693 16. Renner W, Franke WW, Schmid E*, et al.* (1981) Reconstitution of intermediate-sized filaments
694 from denatured monomeric vimentin. *J Mol Biol* 149(2):285-306.
695 17. Lupas A, Van Dyke M & Stock J (1991) Predicting coiled coils from protein sequences.
696 *Science* 252(5009):1162-1164.
697 18. Jumper J, Evans R, Pritzel A*, et al.* (2021) Highly accurate protein structure prediction with
698 AlphaFold. *Nature* 596(7873):583-589.
699 19. Herrmann H, Haner M, Brettel M, Ku NO, & Aebi U (1999) Characterization of distinct early
700 assembly units of different intermediate filament proteins. *J Mol Biol* 286(5):1403-1420.
701 20. Aziz A, Hess JF, Budamagunta MS*, et al.* (2012) The structure of vimentin linker 1 and rod
702 1B domains characterized by site-directed spin-labeling electron paramagnetic resonance
703 (SDSL-EPR) and X-ray crystallography. *J Biol Chem* 287(34):28349-28361.
704 21. Chernyatina AA, Nicolet S, Aebi U, Herrmann H, & Strelkov SV (2012) Atomic structure of the
705 vimentin central alpha-helical domain and its implications for intermediate filament assembly.
706 *Proc Natl Acad Sci U S A* 109(34):13620-13625.
707 22. Ahn J, Jo I, Kang SM*, et al.* (2019) Structural basis for lamin assembly at the molecular level.
708 *Nat Commun* 10(1):3757.
709 23. Eldirany SA, Ho M, Hinbest AJ, Lomakin IB, & Bunick CG (2019) Human keratin 1/10-1B
710 tetramer structures reveal a knob-pocket mechanism in intermediate filament assembly.
711 *EMBO J* 38(11).
712 24. Herrmann H & Aebi U (2004) Intermediate filaments: molecular structure, assembly
713 mechanism, and integration into functionally distinct intracellular Scaffolds. *Annu Rev*
714 *Biochem* 73:749-789.

25. Guzenko D, Chernyatina AA & Strelkov SV (2017) Crystallographic Studies of Intermediate Filament Proteins. *Subcell Biochem* 82:151-170.
26. Eibauer M, Weber MS, Turgay Y*, et al.* (2021) The molecular architecture of vimentin filaments. *BioRxiv*.
27. Eldirany SA, Lomakin IB, Ho M, & Bunick CG (2021) Recent insight into intermediate filament structure. *Curr Opin Cell Biol* 68:132-143.
28. Weber MS, Eibauer M, Sivagurunathan S*, et al.* (2021) Structural heterogeneity of cellular K5/K14 filaments as revealed by cryo-electron microscopy. *Elife* 10.
29. Steinert PM, Marekov LN, Fraser RD, & Parry DA (1993) Keratin intermediate filament structure. Crosslinking studies yield quantitative information on molecular dimensions and mechanism of assembly. *J Mol Biol* 230(2):436-452.
30. Steinert PM, Marekov LN & Parry DA (1993) Diversity of intermediate filament structure. Evidence that the alignment of coiled-coil molecules in vimentin is different from that in keratin intermediate filaments. *Journal of Biological Chemistry* 268(33):24916-24925.
31. Steinert PM, Marekov LN & Parry DA (1993) Conservation of the structure of keratin intermediate filaments: molecular mechanism by which different keratin molecules integrate into preexisting keratin intermediate filaments during differentiation. *Biochemistry* 32(38):10046-10056.
32. Parry DA (1995) Hard alpha-keratin IF: a structural model lacking a head-to-tail molecular overlap but having hybrid features characteristic of both epidermal keratin and vimentin IF. *Proteins* 22(3):267-272.
33. Mucke N, Wedig T, Burer A*, et al.* (2004) Molecular and biophysical characterization of assembly-starter units of human vimentin. *J Mol Biol* 340(1):97-114.
34. Heitlinger E, Peter M, Haner M*, et al.* (1991) Expression of chicken lamin B2 in *Escherichia coli*: characterization of its structure, assembly, and molecular interactions. *J Cell Biol* 113(3):485-495.
35. Parry DAD, Marekov LN & Steinert PM (2001) Subfilamentous Protofibril Structures in Fibrous Proteins. *Journal of Biological Chemistry* 276(42):39253-39258.
36. Goldie KN, Wedig T, Mitra AK*, et al.* (2007) Dissecting the 3-D structure of vimentin intermediate filaments by cryo-electron tomography. *J Struct Biol* 158(3):378-385.
37. Lew MD, Lee SF, Ptacin JL*, et al.* (2011) Three-dimensional superresolution colocalization of intracellular protein superstructures and the cell surface in live *Caulobacter crescentus*. *Proc Natl Acad Sci U S A* 108(46):E1102-1110.
38. Cabeen MT, Murolo MA, Briegel A*, et al.* (2010) Mutations in the Lipopolysaccharide biosynthesis pathway interfere with crescentin-mediated cell curvature in *Caulobacter crescentus*. *J Bacteriol* 192(13):3368-3378.
39. Ingerson-Mahar M, Briegel A, Werner JN, Jensen GJ, & Gitai Z (2010) The metabolic enzyme CTP synthase forms cytoskeletal filaments. *Nat Cell Biol* 12(8):739-746.
40. Dominguez-Escobar J, Chastanet A, Crevenna AH*, et al.* (2011) Processive movement of MreB-associated cell wall biosynthetic complexes in bacteria. *Science* 333(6039):225-228.
41. Garner EC, Bernard R, Wang W*, et al.* (2011) Coupled, circumferential motions of the cell wall synthesis machinery and MreB filaments in *B. subtilis*. *Science* 333(6039):222-225.
42. van Teeffelen S, Wang S, Furchtgott L*, et al.* (2011) The bacterial actin MreB rotates, and rotation depends on cell-wall assembly. *Proc Natl Acad Sci U S A* 108(38):15822-15827.
43. Kelemen GH (2017) Intermediate Filaments Supporting Cell Shape and Growth in Bacteria. *Subcell Biochem* 84:161-211.
44. Pfeiffer D, Toro-Nahuelpan M, Awal RP*, et al.* (2020) A bacterial cytolinker couples positioning of magnetic organelles to cell shape control. *Proc Natl Acad Sci U S A* 117(50):32086-32097.
45. Martin NR, Blackman E, Bratton BP*, et al.* (2021) CrvA and CrvB form a curvature-inducing module sufficient to induce cell-shape complexity in Gram-negative bacteria. *Nat Microbiol* 6(7):910-920.
46. Ely B (1991) Genetics of *Caulobacter crescentus*. *Methods Enzymol* 204:372-384.
47. Soderholm N, Javadi A, Flores IS, Flardh K, & Sandblad L (2018) Affinity to cellulose is a shared property among coiled-coil domains of intermediate filaments and prokaryotic intermediate filament-like proteins. *Sci Rep* 8(1):16524.
48. Zell R & Fritz HJ (1987) DNA mismatch-repair in *Escherichia coli* counteracting the hydrolytic deamination of 5-methyl-cytosine residues. *EMBO J* 6(6):1809-1815.

49. Zheng SQ, Palovcak E, Armache JP*, et al.* (2017) MotionCor2: anisotropic correction of beam-induced motion for improved cryo-electron microscopy. *Nat. Methods* 14(4):331-332.
50. Rohou A & Grigorieff N (2015) CTFFIND4: Fast and accurate defocus estimation from electron micrographs. *J Struct Biol* 192(2):216-221.
51. Bepler T, Kelley K, Noble AJ, & Berger B (2020) Topaz-Denoise: general deep denoising models for cryoEM and cryoET. *Nat Commun* 11(1):5208.
52. Bepler T, Morin A, Rapp M*, et al.* (2019) Positive-unlabeled convolutional neural networks for particle picking in cryo-electron micrographs. *Nat Methods* 16(11):1153-1160.
53. Scheres SH (2012) RELION: implementation of a Bayesian approach to cryo-EM structure determination. *J. Struct. Biol.* 180(3):519-530.
54. Punjani A, Rubinstein JL, Fleet DJ, & Brubaker MA (2017) cryoSPARC: algorithms for rapid unsupervised cryo-EM structure determination. *Nat Methods* 14(3):290-296.
55. Zivanov J, Nakane T & Scheres SHW (2019) A Bayesian approach to beam-induced motion correction in cryo-EM single-particle analysis. *IUCrJ* 6(Pt 1):5-17.
56. Li Y, Zhou M, Hu Q*, et al.* (2017) Mechanistic insights into caspase-9 activation by the structure of the apoptosome holoenzyme. *Proc Natl Acad Sci U S A* 114(7):1542-1547.
57. Scheres SH & Chen S (2012) Prevention of overfitting in cryo-EM structure determination. *Nat. Methods* 9(9):853-854.
58. Rosenthal PB & Henderson R (2003) Optimal determination of particle orientation, absolute hand, and contrast loss in single-particle electron cryomicroscopy. *J. Mol. Biol.* 333(4):721-745.
59. Sanchez-Garcia R, Gomez-Blanco J, Cuervo A*, et al.* (2021) DeepEMhancer: a deep learning solution for cryo-EM volume post-processing. *Commun Biol* 4(1):874.
60. Fang Q, Zhu D, Agarkova I*, et al.* (2019) Near-atomic structure of a giant virus. *Nat Commun* 10(1):388.
61. Guzenko D & Strelkov SV (2018) CCFold: rapid and accurate prediction of coiled-coil structures and application to modelling intermediate filaments. *Bioinformatics* 34(2):215-222.
62. Waterhouse A, Bertoni M, Bienert S*, et al.* (2018) SWISS-MODEL: homology modelling of protein structures and complexes. *Nucleic Acids Res* 46(W1):W296-W303.
63. Pettersen EF, Goddard TD, Huang CC*, et al.* (2004) UCSF Chimera--a visualization system for exploratory research and analysis. *J. Comput. Chem.* 25(13):1605-1612.
64. Emsley P, Lohkamp B, Scott WG, & Cowtan K (2010) Features and development of Coot. *Acta Crystallogr. D Biol. Crystallogr.* 66(Pt 4):486-501.
65. Adams PD, Afonine PV, Bunkoczi G*, et al.* (2010) PHENIX: a comprehensive Python-based system for macromolecular structure solution. *Acta Crystallogr. D Biol. Crystallogr.* 66(Pt 2):213-221.
66. Afonine PV, Poon BK, Read RJ*, et al.* (2018) Real-space refinement in Phenix for cryo-EM and crystallography. *BioRxiv*:249607.
67. Brown JH, Cohen C & Parry DA (1996) Heptad breaks in alpha-helical coiled coils: stutters and stammers. *Proteins* 26(2):134-145.
68. Chen VB, Arendall WB, 3rd, Headd JJ*, et al.* (2010) MolProbity: all-atom structure validation for macromolecular crystallography. *Acta Crystallogr. D Biol. Crystallogr.* 66(Pt 1):12-21.
69. Mastronarde DN (2005) Automated electron microscope tomography using robust prediction of specimen movements. *J Struct Biol* 152(1):36-51.
70. Mastronarde DN & Held SR (2017) Automated tilt series alignment and tomographic reconstruction in IMOD. *J Struct Biol* 197(2):102-113.
71. Kremer JR, Mastronarde DN & McIntosh JR (1996) Computer visualization of three-dimensional image data using IMOD. *J Struct Biol* 116(1):71-76.
72. Agulleiro JI & Fernandez JJ (2015) Tomo3D 2.0--exploitation of advanced vector extensions (AVX) for 3D reconstruction. *J Struct Biol* 189(2):147-152.
73. Ducret A, Quardokus EM & Brun YV (2016) MicrobeJ, a tool for high throughput bacterial cell detection and quantitative analysis. *Nat Microbiol* 1(7):16077.
74. Schindelin J, Arganda-Carreras I, Frise E*, et al.* (2012) Fiji: an open-source platform for biological-image analysis. *Nat Methods* 9(7):676-682.

827 **FIGURES**

828

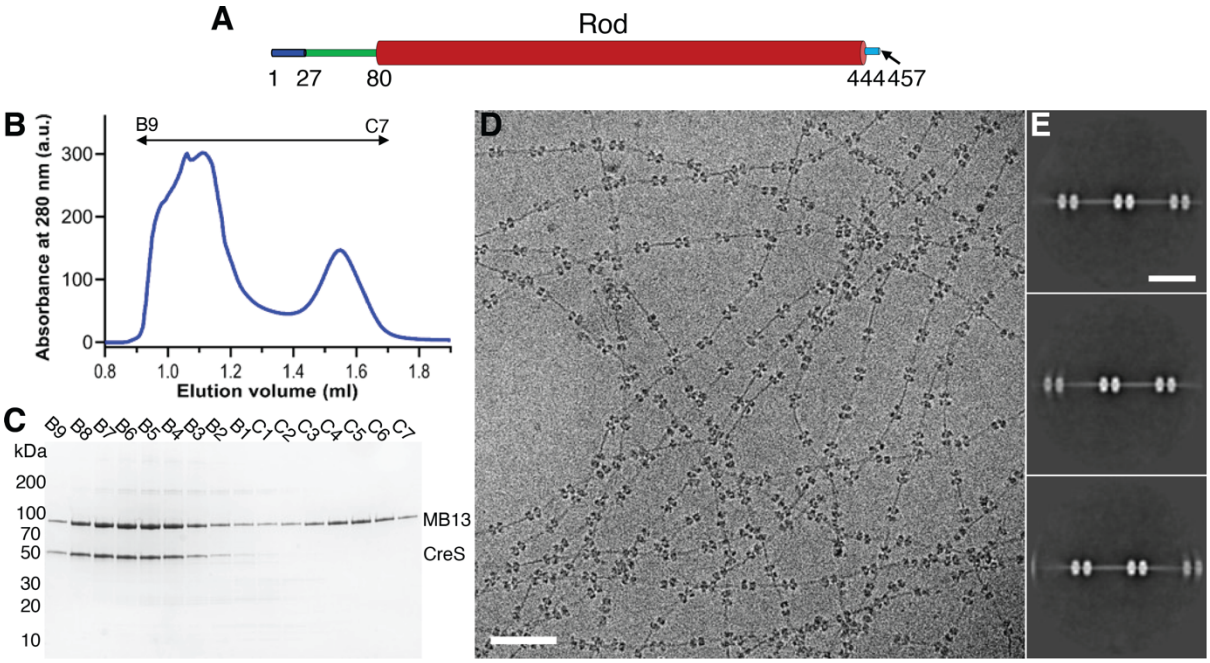

829

830

831 **Figure 1. Production and characterization of a CreS-specific megabody (MB) for structure**
832 **determination of CreS filaments. (A)** Domain organization of full length CreS. The rod domain
833 was defined based on coiled coil prediction [17] and structure prediction using AlphaFold 2 [18]
834 (see **Fig. S1C**). **(B**) Size exclusion chromatography (SEC) profile of $CreS_{sat}$ (a mutant version that
835 has a three amino acid insertion [Ser, Ala and Thr, SAT] before position 406), preincubated with
836 MB13 at 1:4 molar ratio at pH 8. See **Fig. S1D-E** for SEC profile of $CreS_{wt}$ mixed with MB13. (**C**)
837 SDS-PAGE analysis of SEC fractions. Fractions B9 to B5 were pooled and used for EM studies.
838 (**D**) A typical cryo-EM image showing single CreS filaments in complex with MB13 that are formed
839 at pH 6.5. (**D**) Reference-free 2D classification of these filaments reveals a regular spacing of ~60
840 nm between neighbouring “nodes” along the filament. The nodes are caused by MB binding.

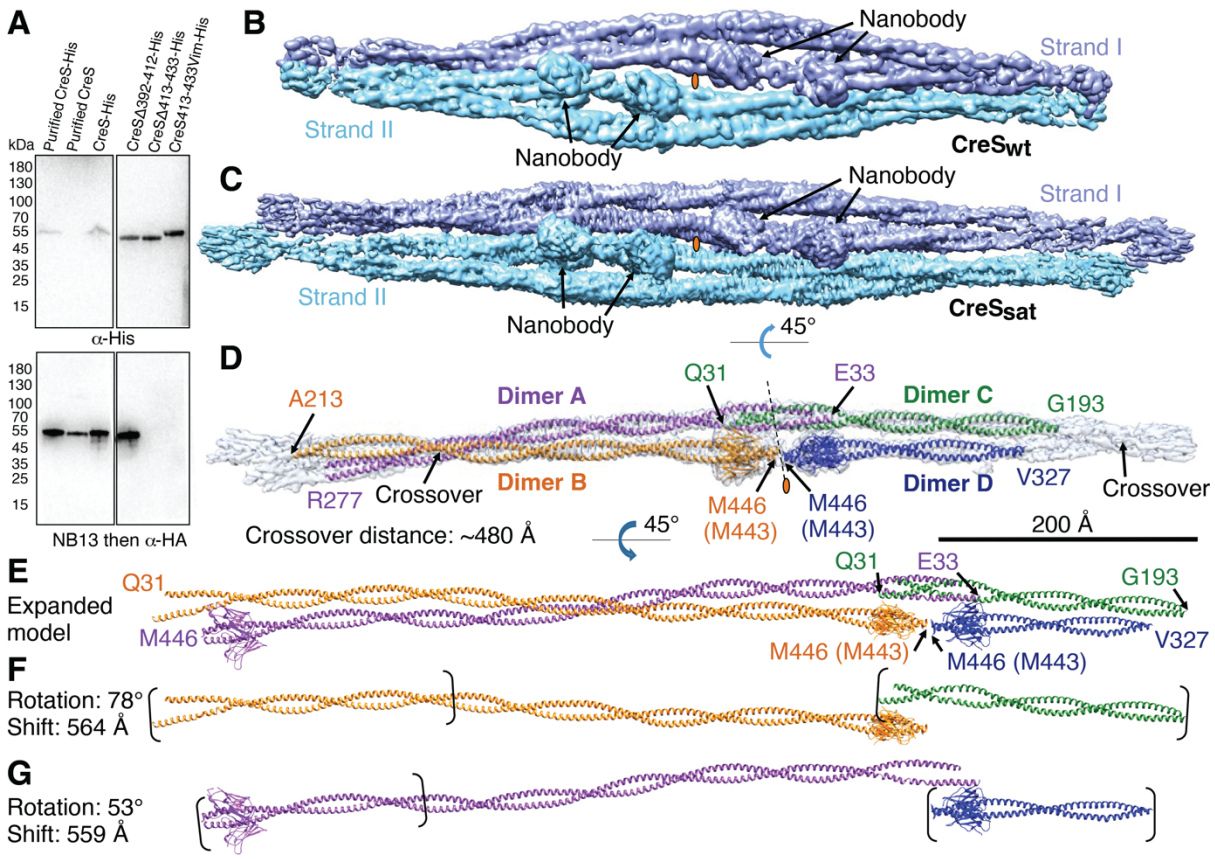

Figure 2. Architecture and assembly of CreS filaments. (**A**) Mapping of the CreS-specific nanobody (NB13) binding region on CreS *in vitro*. All samples except for purified proteins as indicated were cell lysates. The samples were immunoblotted with α-His for analysis of protein expression and with NB13 followed by α-HA for analysis of NB13 binding to CreS. Cryo-EM shows that $CreS_{wt}$ (**B**) and $CreS_{sat}$ (**C**) filaments share a common architecture formed by two strands (shown in cyan and blue) that twist around each other. (**D**) Each strand, with roughly the length of an asymmetric unit shown, consists of two CreS parallel coiled coil dimers that are held together via inter-dimer interactions. (**E**) The expanded atomic model reveals the structure of nearly complete CreS molecules, mostly missing N-terminal residues before Q31 that are presumably disordered. (**F-G**) Transformation of individual CreS dimers along the filament axis in a roughly linear fashion produces the observed single-stranded filamentous assembly. Panels **B-G** are drawn to scale (black scale bar: 200 nm). The positions of pseudo two-fold symmetry axes are indicated by an orange oval. All CreS atomic models shown are of $CreS_{sat}$ throughout all figure panels unless otherwise stated. In these cases, residues are numbered based on $CreS_{sat,}$ whereas residue numbers in parentheses are according to $CreS_{wt.}$

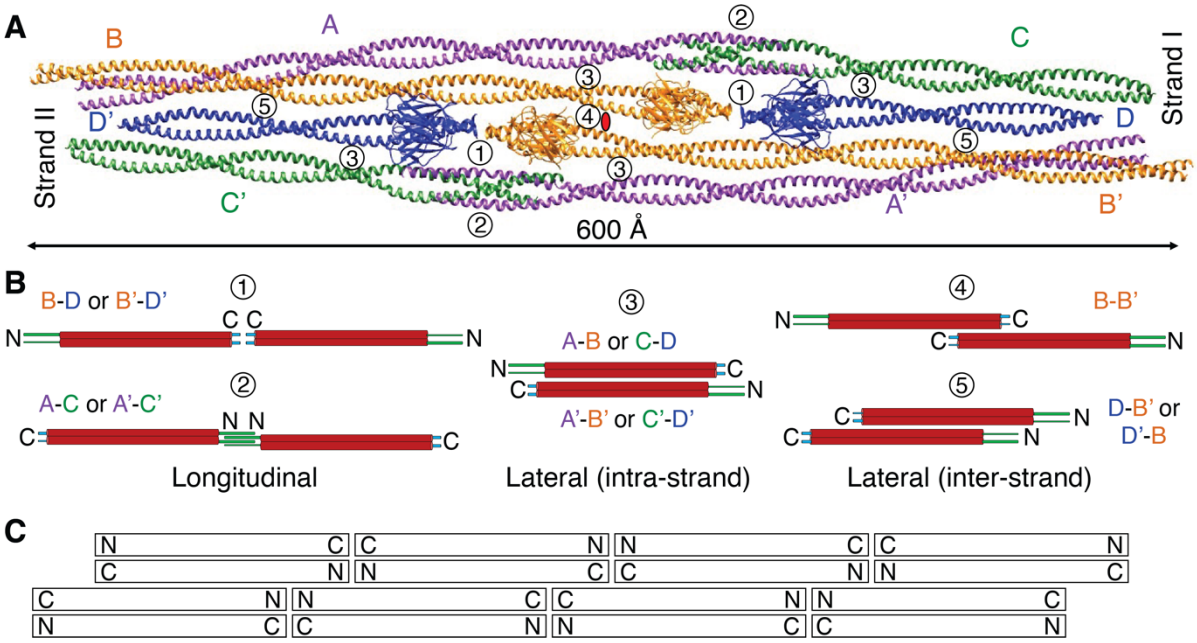

Figure 3. Contacts between CreS coiled coil dimers. (**A**) CreS coiled coil dimers assemble into the two-stranded filament structure via a multitude of longitudinal and lateral inter-dimer interactions that can be classified into five types. (**B**) Schematic representation of the five types of observed dimer-dimer interactions. **(C)** Schematic of the octameric CreS filament, highlighting significant differences to current intermediate filament (IF) models (see also **Fig. S5**).

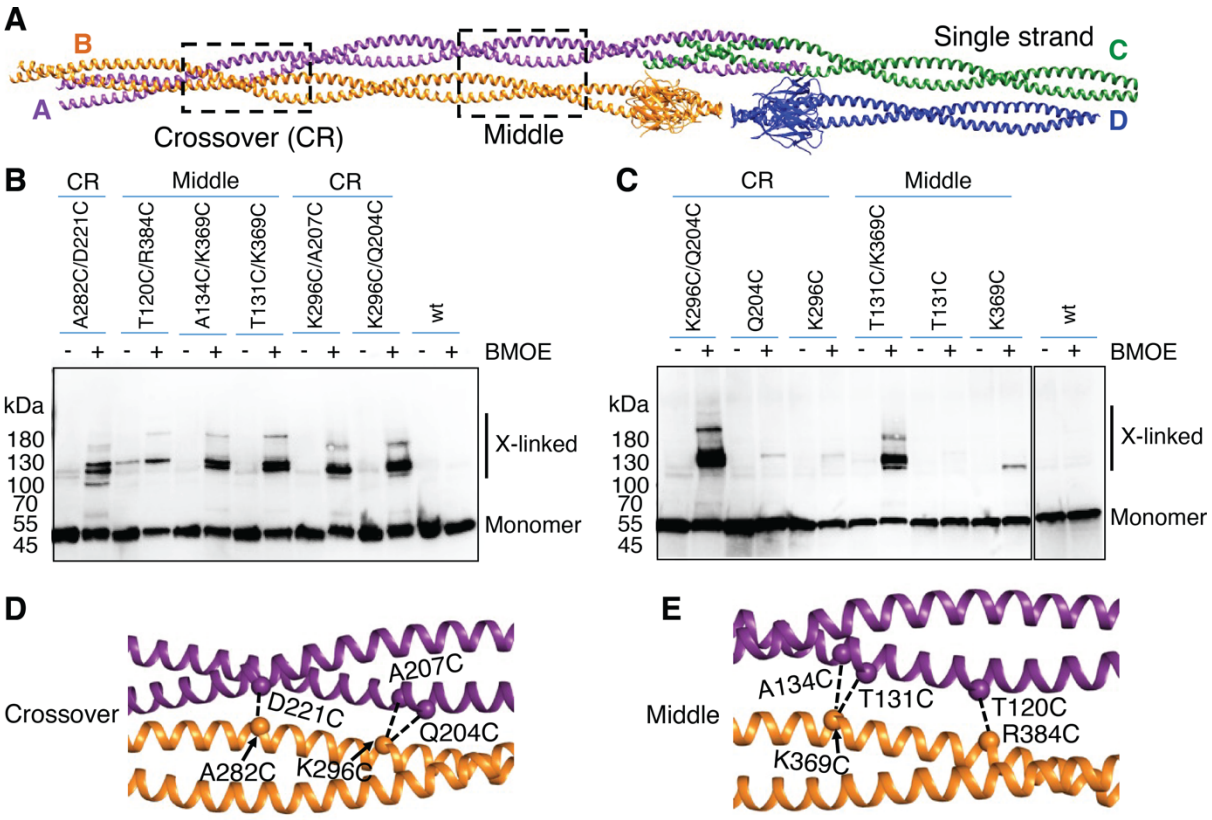

Figure 4. Structure-guided probing of *in vivo* CreS assembly, with a focus on lateral interactions. (A) The single-stranded filament structure of CreS. Dashed rectangles outline the regions in which cysteine substitutions were introduced for *in vivo* crosslinking. (**B-C**) BMOE-dependent cysteine crosslinking of Δ*creS C. crescentus* cells carrying a low-copy-number plasmid expressing *creS* or its cysteine mutants. Reaction products were subjected to Western blotting analysis with a CreS-specific nanobody, NB13. (**D-E**) A close-up view of the regions Crossover (CR, **D**) and Middle (**E**). Cα atoms are shown as spheres. Dashed lines indicate residue-residue pairs probed in **B** and **C**.

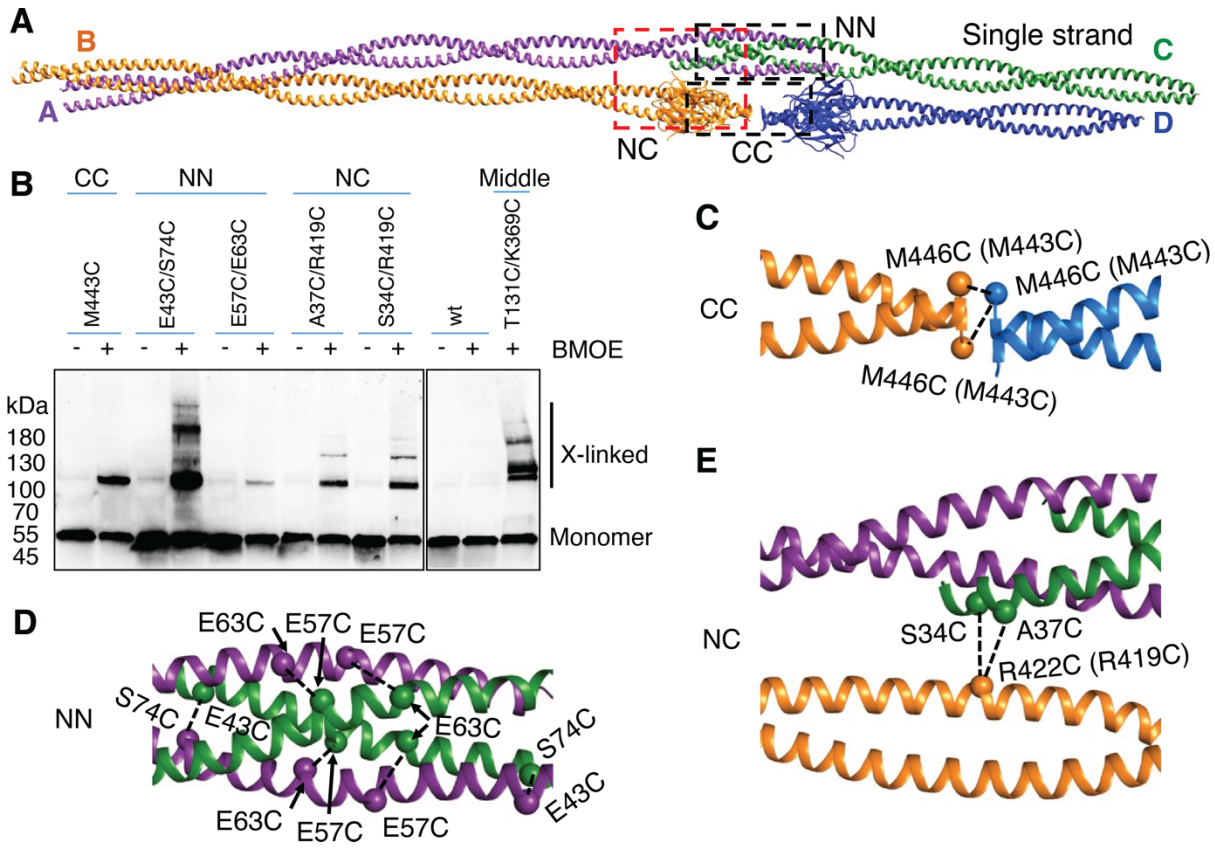

Figure 5. Structure-guided probing of *in vivo* CreS assembly, with a focus on longitudinal interactions. (A) The single-stranded structure of CreS. Dashed rectangles outline the regions where cysteine substitutions were introduced for *in vivo* crosslinking. (**B**) BMOE-mediated cysteine crosslinking of Δ*creS C. crescentus* cells carrying a low-copy-number plasmid expressing *creS* or its cysteine mutants. Reaction products were analysed as described in **Fig. 4B**. (**C-E**) A close-up view of the regions CC (**C**), NN (**D**), and NC (**E**). Cα atoms are shown as spheres. Dashed lines indicate residue-residue pairs probed in **B**. As in **Fig. 1**, residues in **C** and **E** are numbered based on $CreS_{sat}$, whereas residue numbers in parentheses are according to $CreS_{wt}$.

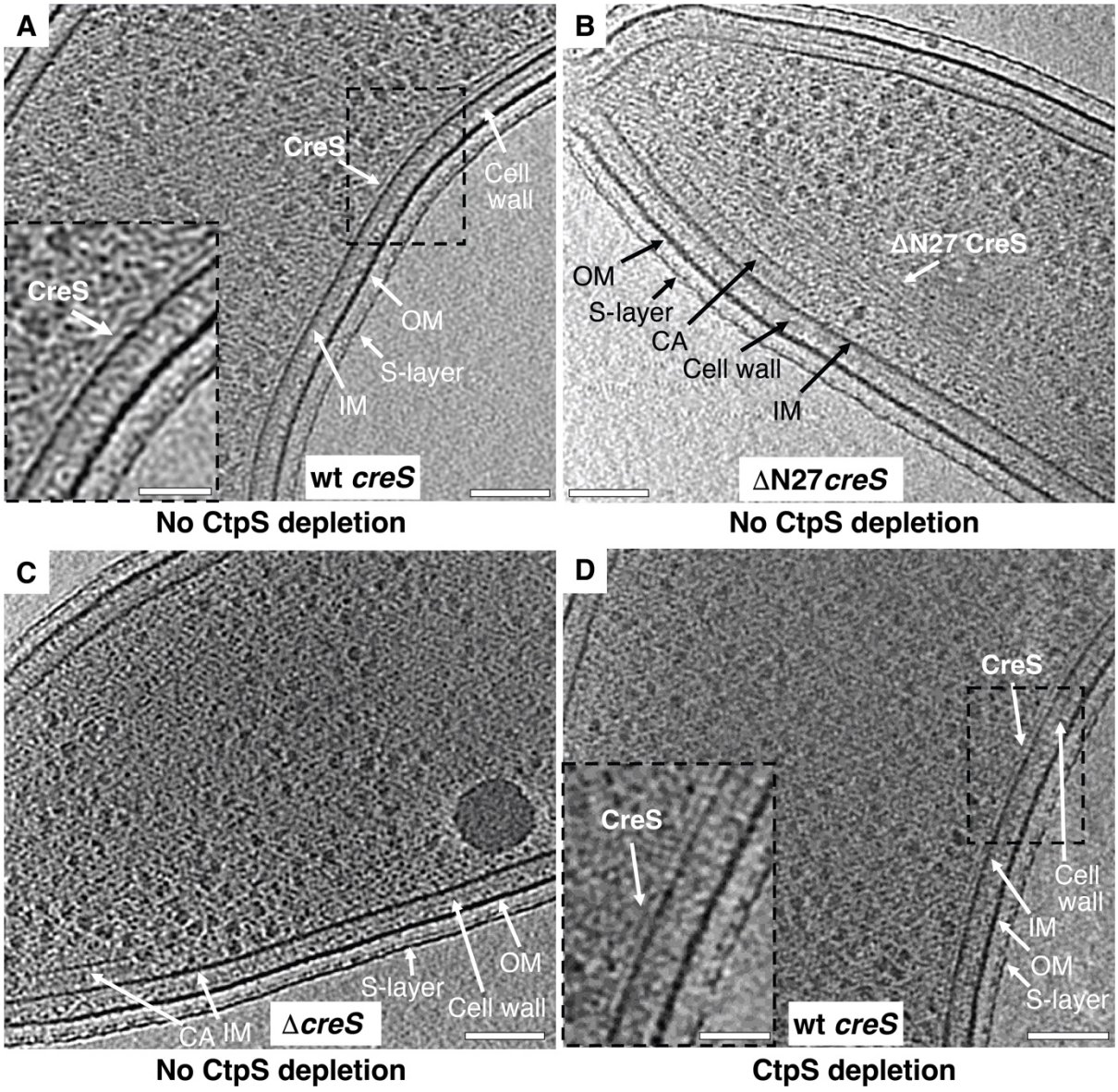

Figure 6. Subcellular organization of CreS filaments in cells. Tomographic slices through wild-type (wt) *C. crescentus* cells with wt *creS* overexpression (**A**, strain CJW1430), Δ*creS* cells with ΔN27 *creS* overexpression (**B**, strain YL006), Δ*creS* cells (**C**, strain LS2813), and Δ*creS* cells with both CtpS depletion and wt *creS* overexpression (**D**, strain YL062). Scale bar: 100 nm. The insets (scale bar: 200 nm) in **A** and **D** show a close-up view of the area outlined by the dashed rectangle. IM: inner cell membrane; CA: chemosensory array; OM: outer membrane.

894 **SUPPLEMENTARY FIGURES**

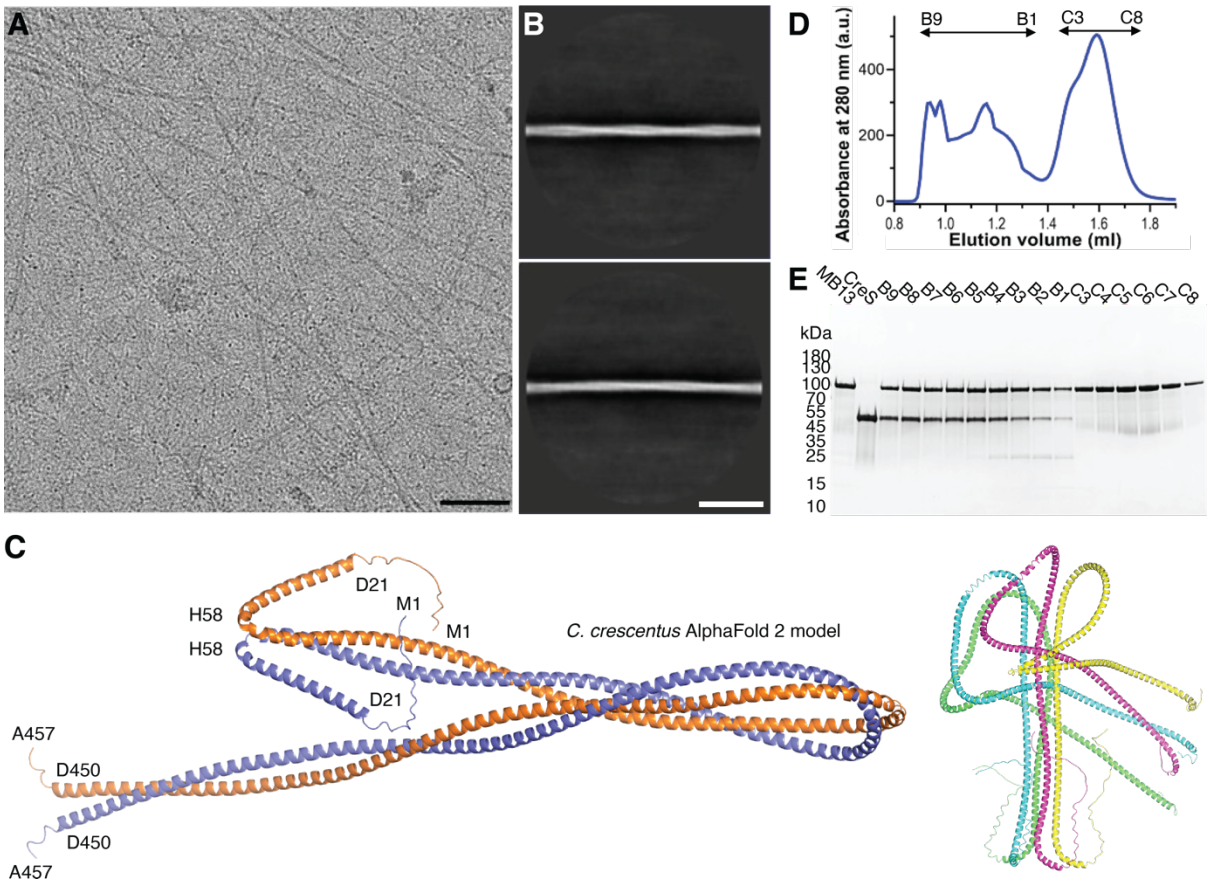

895

896

897 **Figure S1.** CreS$_{wt}$ assembles into two-stranded filaments *in vitro*. (**A**) Cryo-EM micrograph of
898 single filaments of CreS$_{wt}$ formed at pH 7. (**B**) Two-dimensional (2D) class averages show the
899 presence of two intertwined strands. Scale bar: 100 nm (**A**) and 50 nm (**B**). Megabody MB13 forms
900 a complex with CreS$_{wt}$. **(C)** Left: annotated AlphaFold 2 model of CreS dimer. Right: AlphaFold 2
901 model of CreS tetramer. (**D**) Size exclusion chromatography (SEC) profile of CreS$_{wt}$, preincubated
902 with an excess of MB13 (1:4 molar ratio) at pH 8. (**E**) SDS-PAGE analysis of SEC fractions.
903 Fractions B9 to B5 were pooled and used for EM analysis. MB13 top, CreS$_{wt}$ bottom bands.

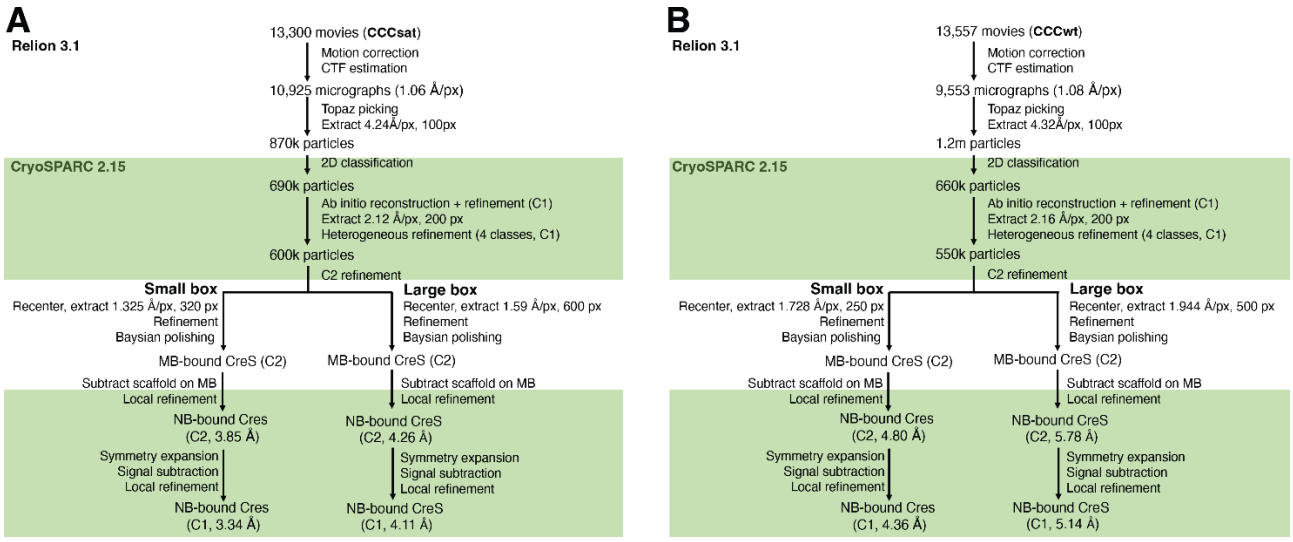

Figure S2. Cryo-EM structure determination of CreS. Image processing workflow used for $CreS_{sat}$ (**A**) and $CreS_{wt}$ (**B**).

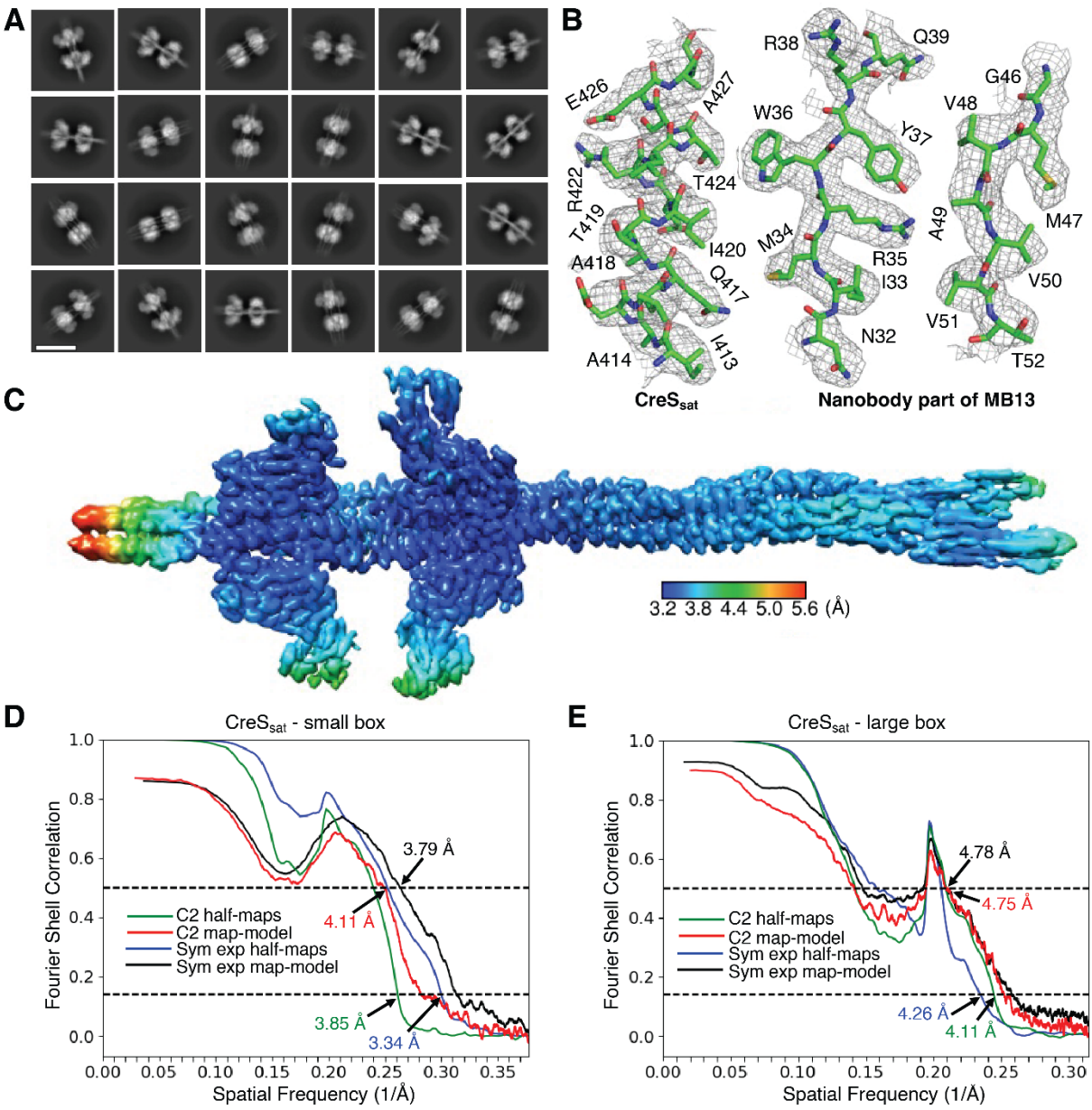

Figure S3. Cryo-EM analysis of $CreS_{sat}$ filaments in complex with megabody MB13. Related to **Figure 2**. (**A**) 2D class averages of individual nodes formed by MB13 and $CreS_{sat}$ in different orientations. (**B**) Typical cryo-EM map densities for $CreS_{sat}$ and MB13, with the fitted atomic model superimposed. (**C**) Local resolution of the symmetry-expanded map reconstructed with a box size of 424 Å. FSC-based resolution estimation for maps reconstructed using a box size of 424 Å (**D**, small box) and 960 Å (**E**, large box).

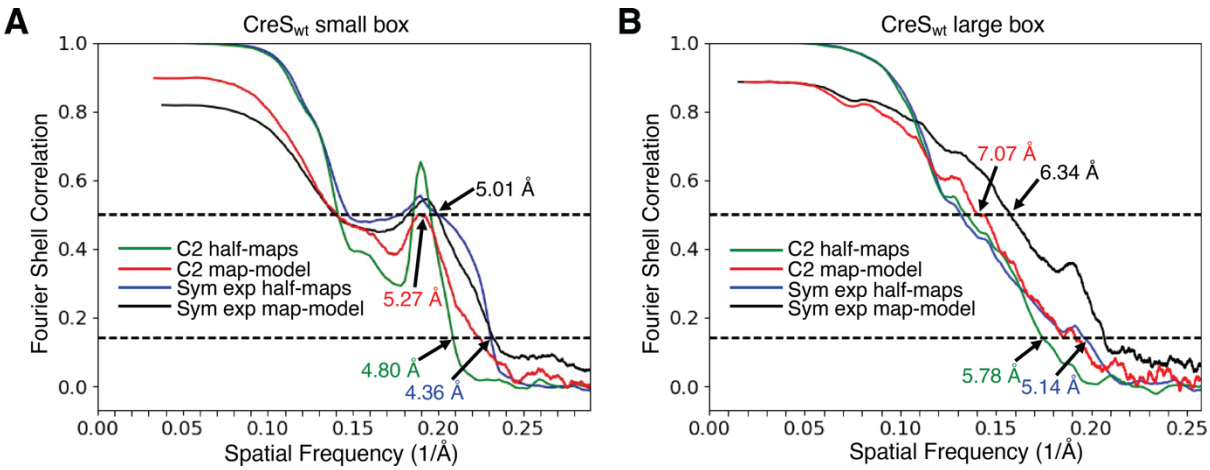

Figure S4. Cryo-EM analysis of $CreS_{wt}$ filaments in complex with megabody MB13. Related to **Fig. 2.** Resolution estimation for maps reconstructed using a box size of 432 Å (**A**, small box) and 972 Å (**B**, large box) based on FSC curves.

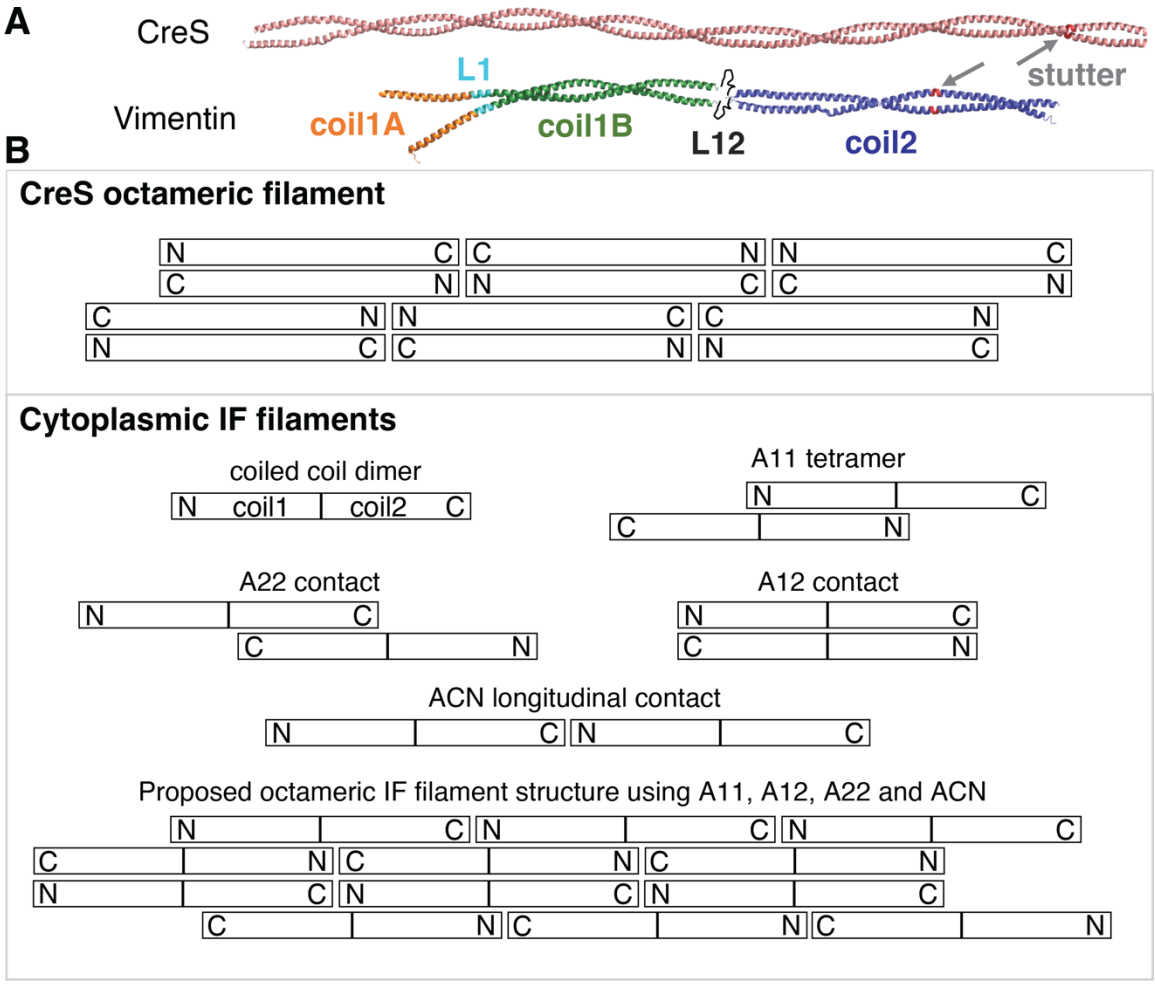

Figure S5. Structural comparison of CreS with eukaryotic IF proteins. (**A**) To-scale comparison of the atomic model of a CreS dimer (upper) with the composite atomic model of a vimentin dimer (lower). The IF structure shown is a hybrid model assembled from crystal structures of vimentin fragments (PDB entries 1GK4, 3S4R, 3TRT, 3UF1, and 1GK6), similar to what was reported [21]. (**B**) Comparison of crescentin filaments (upper box, same as **Fig. 3C**) with current models of cytoplasmic IF protein filaments (lower box). IF proteins also form parallel and extended coiled coil dimers. Many IF proteins have been shown to form staggered and antiparallel "A11" tetramers, in which two dimers come together via their coil1 rod segments. IF polymers have also been shown, mostly by cross-linking studies, to contain staggered A22 and flush A12 contacts. End-to-end contacts are believed to be via N- and C-terminal ends coming together, head-to-tail ACN contacts. There is little experimental evidence for ACN contacts in cytoplasmic IF filaments, but it is difficult to build gap-free models using the other contacts, without ACN contacts. The current model of an IF "octameric" protofilament is shown at the bottom [11]. The most striking difference to the structure of crescentin filaments discovered here is that all longitudinal contacts are head-to-tail (N-C) in IFs (ACN), and not N-N and C-C head-to-head and head-to-tail, as in crescentin. Both

filaments lack overall polarity and one inter-dimer contact is similar, A12 and interaction type 3 **(Fig. 3A & C)**, whereas the others are different. For example, there is no parallel inter-dimer contact in the IF model, as in crescentin's interaction type 5 **(Fig. 3A & C)**. Furthermore, A11 and A22 in IF filaments are more substantial than the somewhat related contact types 2 (N-N) and 4 (C-C overlap) in crescentin, respectively (**Fig. 3A & C)**. While somewhat related in overall architecture, the way the dimers come together to form filaments can be described as significantly different.

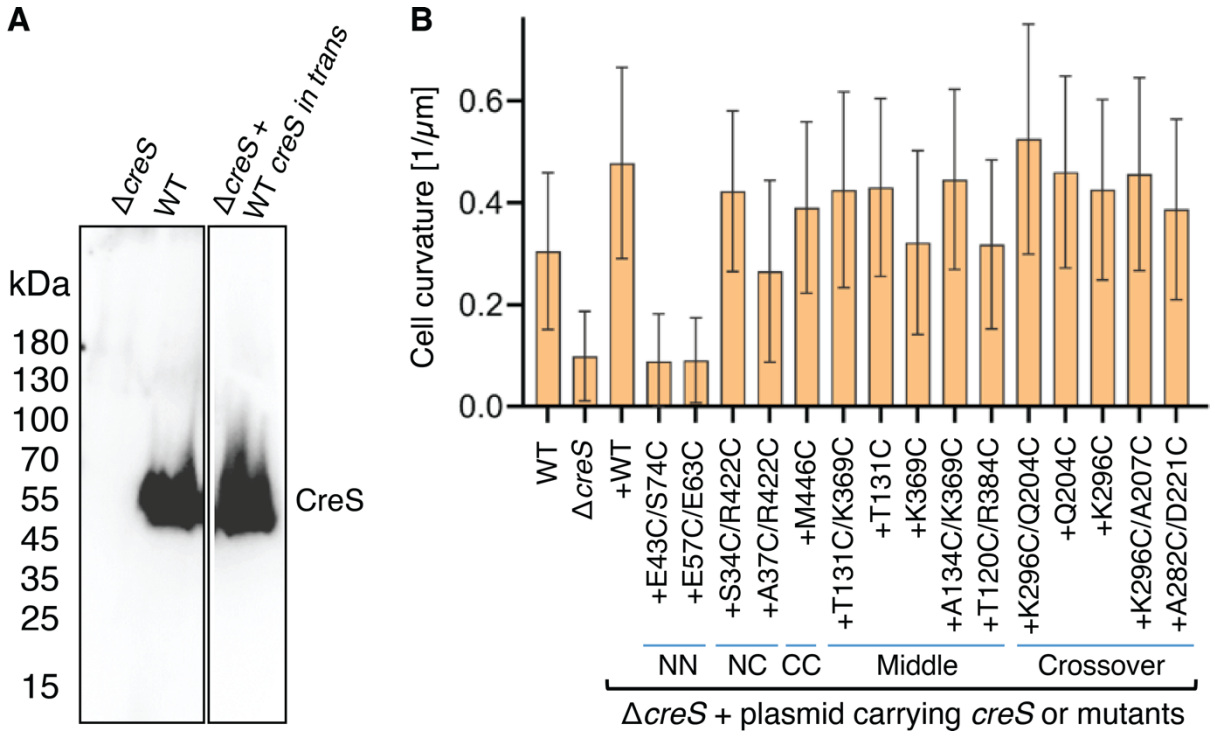

Figure S6. Characterization of *C. crescentus* cells carrying a *creS*-expressing plasmid. (**A**) Western blotting analysis of CreS protein levels in *C. crescentus* strains. Production of CreS from a low-copy-number plasmid under its native promoter in a *creS* deletion background yields a similar protein level as that in the wt strain. (**B**) Quantification of cell curvature of *C. crescentus* strains used for cysteine crosslinking experiments (as in **Figs 4-5**). The mean curvature values are shown, and error bars represent standard deviations. The number of cells analysed for each strain was between 114 and 591.

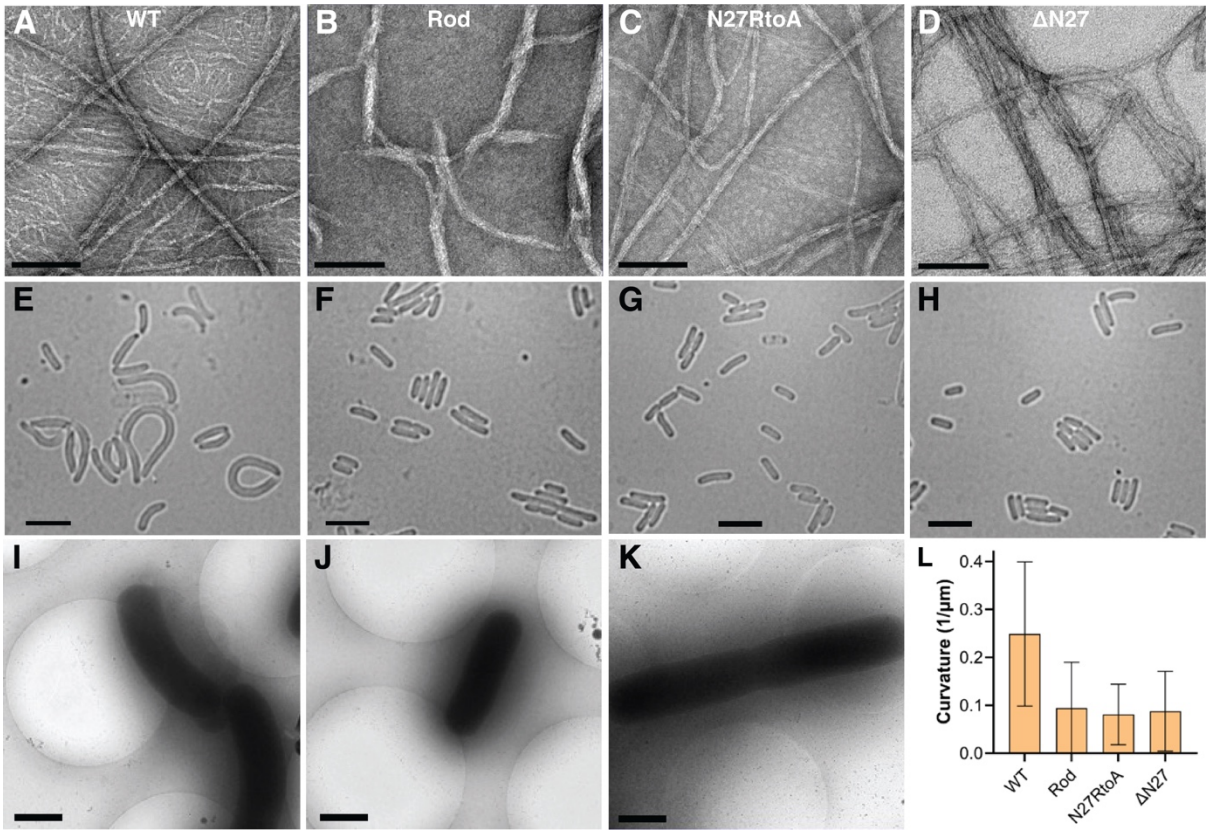

Figure S7. The N-terminal residues 1-27 of CreS are required for its cell shape function in *E. coli*. (**A-D**) EM micrographs of negatively stained filaments formed *in vitro* using purified $CreS_{wt}$ (**A**), $CreS_{rod}$ (**B**), $CreS_{N27RtoA}$, where all Arg residues were substituted with an Ala in the N-terminal 27 amino acids (**C**), and $CreS_{\Delta N27}$ (**D**). Scale bar: 100 nm. (**E-J**) Typical phase contrast images of *E. coli* cells overexpressing $CreS_{wt}$ (**E**), $CreS_{rod}$ (**F**), $CreS_{N27RtoA}$ (**G**), and $CreS_{\Delta N27}$ (**H**). Scale bar: 5 μm. (**I-K**) Typical cryo-EM images of *E. coli* cells overexpressing $CreS_{wt}$ (**I**), $CreS_{rod}$ (**J**), and $CreS_{N27RtoA}$ (**K**). Scale bar: 1 μm. (**L**) Quantification of cell curvature based on phase contrast images (corresponding to panels **E-J**). Shown are the mean curvature values with error bars representing standard deviations. The numbers of cells analysed for each strain were between 140 and 293. Protein expression was induced by 0.05 mM IPTG for ~2.5 h.

969 **SUPPLEMENTARY TABLES**

970 **Table S1. Strains and plasmids**

Name	Description/Genotype	Source
Strains		
E. coli		
BL21 (DE3)	F– *ompT hsdSB (rB- mB-) gal dcm* (DE3)	NEB
C41 (DE3)	F– *ompT hsdSB (rB- mB-) gal dcm* (DE3)	Sigma-Aldrich
WK6	F' *lacIq* Δ(*lacZ*)M15 *proA+B+* Δ(*lac-proAB*) *galE rpsL*	VIB
CJW1659	BL21 (DE3) expressing $CreS_{wt}$ (non-tagged)	[1]
CJW1661	C41 (DE3) expressing $CreS_{wt}$ (non-tagged)	[1]
CJW2045	BL21 (DE3) expressing $CreS_{sat}$ (insertion of three amino acids (Ser, Ala, SAT, at position 406)	[1]
C. crescentus (vibrioides)		
CB15N	Synchronizable strain of CB15	[2]
LS2813	CB15N Δ*creS*	[3]
ZG216	CB15N Δ*creS ctpS*1-400 P_{xylX}-*ctpS* (*ctpS* truncated to first 400 bp and another *ctpS* under a xylose inducible promoter on chromosome)	[4]
CJW1430	CB15N + pJS14-based medium-copy-number plasmid for expressing CreS under its native promoter	[5]
YL010	CB15N Δ*creS* + pCT133-P_{cres}-$CreS_{wt}$	This study
YL006	CB15N Δ*creS* + pCT133-P_{cres}-$CreS_{\Delta N27}$	This study
YL012	CB15N Δ*creS* + pCT133-P_{cres}-$CreS_{M443C}$	This study
YL017	CB15N Δ*creS* + pCT133-P_{cres}-$CreS_{E43C+S74C}$	This study
YL018	CB15N Δ*creS* + pCT133-P_{cres}-$CreS_{E57C+E63C}$	This study
YL019	CB15N Δ*creS* + pCT133-P_{cres}-$CreS_{R419C+S34C}$	This study
YL020	CB15N Δ*creS* + pCT133-P_{cres}-$CreS_{R419C+A37C}$	This study
YL022	CB15N Δ*creS* + pCT133-P_{cres}-$CreS_{K369C+T131C}$	This study
YL023	CB15N Δ*creS* + pCT133-P_{cres}-$CreS_{K369C+A134C}$	This study
YL024	CB15N Δ*creS* + pCT133-P_{cres}-$CreS_{R384C+T120C}$	This study
YL025	CB15N Δ*creS* + pCT133-P_{cres}-$CreS_{K296C+Q204C}$	This study
YL026	CB15N Δ*creS* + pCT133-P_{cres}-$CreS_{K296C+A207C}$	This study
YL027	CB15N Δ*creS* + pCT133-P_{cres}-$CreS_{A282C+D221C}$	This study
YL031	CB15N Δ*creS* + pCT133-P_{cres}-$CreS_{Q204C}$	This study
YL032	CB15N Δ*creS* + pCT133-P_{cres}-$CreS_{K296C}$	This study
YL033	CB15N Δ*creS* + pCT133-P_{cres}-$CreS_{T131C}$	This study
YL034	CB15N Δ*creS* + pCT133-P_{cres}-$CreS_{K369C}$	This study
YL062	ZG216 + pCT155-P_{cres}-$CreS_{WT}$	This study
Plasmids		
pCT155-P_{van}-*3xM2-didA*	pCT155-based parental plasmid for cloning (medium copy number, pJS14-based, $chlor^R$)	[6]
pCT133-P_{van}-*3xM2-didA*	pCT133-based parental plasmid for cloning (low copy number, pMR20-based, tet^R)	[6]
pHis17-CreSΔN27	pHis17-based plasmid for expressing $CreS_{\Delta N27}$ (residues 28-457)	This study
pHis17-CreSN274RtoA	pHis17-based plasmid for expressing $CreS_{N27RtoA}$ (all Arg mutated to Ala in residues 1-27)	This study
pHis17-CreSRod	pHis17-based plasmid for expressing $CreS_{Rod}$ (residues 80-444)	This study
pFE127	pHis17-based plasmid for expressing CreS-His ($CreS_{wt}$ followed by GSHHHHHH)	This study

pHis17-CreSΔ392-412-His	pHis17-based plasmid for expressing $CreS_{\Delta 392-412}$-His (residues 392-412 deleted)	This study
pHis17-CreSΔ413-433-His	pHis17-based plasmid for expressing $CreS_{\Delta 413-433}$-His (residues 413-433 deleted)	This study
pHis17-CreS413-433Vim-His	pHis17-based plasmid for expressing $CreS_{413-433Vim}$-His (residues 413-433 replaced by the homologous region in human vimentin)	This study
pMECS-NB13-HA-His	pMECS-based phagemid for expressing NB13-HA-His, a CreS-specific nanobody followed an HA tag and a 6x His tag	This study (provided by VIB)
pET-22b-MB13-His	pET-22b based plasmid for expressing MB13-His, a CreS-specific megabody with a C-terminal a 6x His tag	This study
pCT133-P_{cres}-$CreS_{wt}$	pCT133 based plasmid for expressing $CreS_{wt}$ under its native promoter	This study
pCT133-P_{cres}-$CreS_{\Delta N27}$	pCT133 based plasmid for expressing $CreS_{\Delta N27}$ (aa 1-27 deleted) under its native promoter	This study
pCT133-P_{cres}-$CreS_{M443C}$	pCT133 based plasmid for expressing $CreS_{M443C}$ under its native promoter	This study
pCT133-P_{cres}-$CreS_{E43C+S74C}$	pCT133 based plasmid for expressing $CreS_{E43C+S74C}$ under its native promoter	This study
pCT133-P_{cres}-$CreS_{E57C+E63C}$	pCT133 based plasmid for expressing $CreS_{E57C+E63C}$ under its native promoter	This study
pCT133-P_{cres}-$CreS_{R419C+S34C}$	pCT133 based plasmid for expressing $CreS_{R419C+S34C}$ under its native promoter	This study
pCT133-P_{cres}-$CreS_{R419C+A37C}$	pCT133 based plasmid for expressing $CreS_{R419C+A37C}$ under its native promoter	This study
pCT133-P_{cres}-$CreS_{K369C+T131C}$	pCT133 based plasmid for expressing $CreS_{K369C+T131C}$ under its native promoter	This study
pCT133-P_{cres}-$CreS_{K369C+A134C}$	pCT133 based plasmid for expressing $CreS_{K369C+A134C}$ under its native promoter	This study
pCT133-P_{cres}-$CreS_{R384C+T120C}$	pCT133 based plasmid for expressing $CreS_{R384C+T120C}$ under its native promoter	This study
pCT133-P_{cres}-$CreS_{K296C+Q204C}$	pCT133 based plasmid for expressing $CreS_{K296C+Q204C}$ under its native promoter	This study
pCT133-P_{cres}-$CreS_{K296C+A207C}$	pCT133 based plasmid for expressing $CreS_{K296C+A207C}$ under its native promoter	This study
pCT133-P_{cres}-$CreS_{A282C+D221C}$	pCT133 based plasmid for expressing $CreS_{A282C+D221C}$ under its native promoter	This study
pCT133-P_{cres}-$CreS_{Q204C}$	pCT133 based plasmid for expressing $CreS_{Q204C}$ under its native promoter	This study
pCT133-P_{cres}-$CreS_{K296C}$	pCT133 based plasmid for expressing $CreS_{K296C}$ under its native promoter	This study
pCT133-P_{cres}-$CreS_{T131C}$	pCT133 based plasmid for expressing $CreS_{T131C}$ under its native promoter	This study
pCT133-P_{cres}-$CreS_{K369C}$	pCT133 based plasmid for expressing $CreS_{K369C}$ under its native promoter	This study
pCT155-P_{cres}-$CreS_{WT}$	pCT155 based plasmid for expressing $CreS_{wt}$ under its native promoter	This study

971

Table S2. Amino acid sequences of proteins used in this study

CreS *Caulobacter crescentus* crescentin (GenBank accession identifier: ACL97278.1)

MRLLSKNSRETKNGKPTVLGDEARAEAMQHQIESTQAIGQRYETIHGGLDSIGRVMEHLKAIEPLIAEIRG
PVSQEFEARRAEHAELIAVRANLDQAQRQIALIQAEEREVSARLAAAETALGESDARRQTQDAALEDNALE
IDRLRNALLQSDLKVSSLDASLRDATARIEHLVQDVEGLRVQAQDIDARRGDAEAALARANQDNALLGEEA
ATLKKRVDQAGLDLARLSRIETDLEAQLAAERARVQAVENALAAHQADSGRTIRGLESQVEANRAEISALQ
TRLETATGRADKLEEMNGQISARLADSSAQQKAVERRAGDLNVALERALDRIRALEEEADGLRQRHAGVDT
ARATAIERADQLAKSAVAQEKALKRAEERAQQLRARLDAMQEAQDQVRRDHEAKIAELQATIERLTSEAAL
AEGALEAARRDRSRLQMALLGASDGDVAASA

CreS stutter mutant (SAT insertion before 406)

MRLLSKNSRETKNGKPTVLGDEARAEAMQHQIESTQAIGQRYETIHGGLDSIGRVMEHLKAIEPLIAEIRG
PVSQEFEARRAEHAELIAVRANLDQAQRQIALIQAEEREVSARLAAAETALGESDARRQTQDAALEDNALE
IDRLRNALLQSDLKVSSLDASLRDATARIEHLVQDVEGLRVQAQDIDARRGDAEAALARANQDNALLGEEA
ATLKKRVDQAGLDLARLSRIETDLEAQLAAERARVQAVENALAAHQADSGRTIRGLESQVEANRAEISALQ
TRLETATGRADKLEEMNGQISARLADSSAQQKAVERRAGDLNVALERALDRIRALEEEADGLRQRHAGVDT
ARATAIERADQLAKSAVAQEKALKRAEERAQQLRARLDAMQEAQDQVRRDSATHEAKIAELQATIERLTSE
AALAEGALEAARRDRSRLQMALLGASDGDVAASA

Nanobody NB13 (HA-tag, 6×His-tag)

QVQLQESGGGLVQTGGSLRLSCASSRSIDGINIMRWYRQAPGKQRGMVAVVTGWGSTNYVDSVKGRFIISR
DSAKDTVYLQMNNLKPEDTAVYSCNAIYRGSEYWGQGTQVTVSSAAAYPYDVPDYGSHHHHHH

Megabody MB13 (NB13, YgjK, 10×His-tag)

EVQLQESGGGLVYKEETQSGLNNYARVVEKGQYDSLEIPAQVAASWESGRDDAAVFGFIDKEQLDKYVANG
GKRSDWTVKFAENRSQDGTLLGYSLLQESVDQASYMYSDNHYLAEMATILGKPEEAKRYRQLAQQLADYIN
TCMFDPTTQFYYDVRIEDKPLANGCAGKPIVERGKGPEGWSPLFNGAATQANADAVVKVMLDPKEFNTFVP
LGTAALTNPAFGADIYWRGRVWVDQFWFGLKGMERYGYRDDALKLADTFFRHAKGLTADGPIQENYNPLTG
AQQGAPNFSWSAAHLYMLYNDFFRKQASGGGSGGGGSGGGGSGNADNYKNVINRTGAPQYMKDYDYDDHQR
FNPFFDLGAWHGHLLPDGPNTMGGFPGVALLTEEYINFMASNFDRLTVWQDGKKVDFTLEAYSIPGALVQK
LTAKDVQVEMTLRFATPRTSLLETKITSNKPLDLVWDGELLEKLEAKEGKPLSDKTIAGEYPDYQRKISAT
RDGLKVTFGKVRATWDLLTSGESEYQVHKSLPVQTEINGNRFTSKAHINGSTTLYTTYSHLLTAQEVSKEQ
MQIRDILARPAFYLTASQQRWEEYLKKGLTNPDATPEQTRVAVKAIETLNGNWRSPGGAVKFNTVTPSVTG
RWFSGNQTWPWDTWKQAFAMAHFNPDIAKENIRAVFSWQIQPGDSVRPQDVGFVPDLIAWNLSPERGGDGG
NWNERNTKPSLAAWSVMEVYNVTQDKTWVAEMYPKLVAYHDWWLRNRDHNGNGVPEYGATRDKAHNTESGE
MLFTVKKDSLRLSCASSRSIDGINIMRWYRQAPGKQRGMVAVVTGWGSTNYVDSVKGRFIISRDSAKDTVY
LQMNNLKPEDTAVYSCNAIYRGSEYWGQGTQVTVSSGENLYFQGSHHHHHHHHHH

1008 **Table S3. Cryo-EM data collection and processing statistics**

	$CreS_{sat}$				**$CreS_{wt}$**			
	Small box		Large box		Small box		Large box	
	SAT-SB-C2	SAT-SB-C1	SAT-LB-C2	SAT-LB-C1	WT-SB-C2	WT-SB-C1	WT-LB-C2	WT-LB-C1
EMDB ID	EMD-15398	EMD-15395	EMD-15476	EMD-15446	EMD-15402	EMD-15401	EMD-15473	EMD-15465
PDB ID	8AFH	8AFE	8AJB	8AHL	8AFM	8AFL	8AIX	8AIA
Data collection and processing								
Microscope	Titan Krios IV (eBIC)				Titan Krios II (MRC LMB)			
Accelerating voltage (kV)	300				300			
Camera	Gatan K3				Falcon IV			
Micrographs (collected/selected)	13330 / 10925				13557 / 9553			
Nominal magnification	81000x				75000x			
Pixel size (Å/pixel)	0.53[a]				1.08			
Dose rate (e^-/pixel/s)	25				4			
Total exposure ($e^-/Å^2$)	53				34			
Frame rate (ms)	60				4 (EER - electron event representation)			
No. of frames	40				2410			
Defocus (µm)	0.4-2.6				0.4-4.0			
No. of particels (extraction)	869812				1211745			
No. of particels (reconstruction)	599993	1199985	585252	1170504	550575	1101149	550574	1101148
Map resolution (half-map)[b] (Å)	3.85	3.34	4.26	4.11	4.8	4.36	5.78	5.14
Map resolution (model-map)[c] (Å)	4.11	3.79	4.78	4.75	5.27	5.01	7.07	6.34
Pixel size (reconstruction, Å/px)	1.325	1.325	1.59	1.59	1.728	1.728	1.944	1.944
Box size (reconstruction, px)	320	320	600	600	250	250	500	500
Point group symmetry	C2	C1	C2	C1	C2	C1	C2	C1
Model Statistics								
Model-map correlation coeffcient[d] - CC_{volume}/CC_{mask}	0.70/0.66	0.70/0.685	0.64/0.55	0.70/0.64	0.64/0.60	0.66/0.63	0.69/0.67	0.71/0.67
No. of atoms								
Protein	13578	6789	30112	15056	7846	3923	21930	10965

R.m.s deviations[e]								
Bond lengths (Å)	0.006	0.006	0.007	0.006	0.005	0.004	0.007	0.007
Bond angles (°)	0.981	0.677	1.251	1.019	0.995	0.723	1.265	1.072
Ramachadran plot[e]								
Favored (%)	95.1	95.1	95.2	95.2	91.6	91.6	89.2	89.2
Allowed (%)	4.9	4.9	4.8	4.8	8.4	8.4	10.8	10.8
Outliers (%)	0.0	0.0	0.0	0.0	0.0	0.0	0.0	0.0
Rotamer outliers[e]	0.00	0.00	0.13	0.13	0.25	0.25	0.09	0.09
Clash score[e]	14.81	13.85	29.63	29.56	17.91	18.17	48.71	48.51
Molprobity score[e]	2.02	1.99	2.29	2.29	2.25	2.26	2.74	2.73
Cβ outliers[e]	0.0	0.0	0.0	0.0	0.0	0.0	0.0	0.0

[a] Super resolution pixel size. The physical pixel size is 1.06 Å/pixel.

[b] Based on FSC between two independently calculated half maps (FSC cutoff 0.143) [7, 8].

[c] Based on model-map FSC between the cryo-EM map and a map calculated based on the atomic model specifying the cryo-EM map resolution (FSC cutoff 0.5) [7].

[d] Atomic coordinates were refined against the cryo-EM map in real space using Phenix [9]. CC_{mask} and CC_{volume} are defined as in [10].

[e] Based on the criteria of MolProbity [11].

1020 **Table S4. Comparison of residue-residue contacts between $CreS_{sat}$ and $CreS_{wt}$.**

Region	Type	Residue A[a]	Residue B[a]	$CreS_{wt}$[b] (Å)	$CreS_{sat}$[b] (Å)
Middle	Inter-dimer, lateral	K369	T131	8 (9)	8 (9)
Middle	Intra-dimer	K369	K369	17 (15)	16 (14)
Middle	Intra-dimer	T131	T131	16 (15)	15 (14)
Middle	Inter-dimer, lateral	K369	A134	7 (10)	8 (10)
Middle	Inter-dimer, lateral	R384	T120	8 (10)	8 (9)
Crossover	Inter-dimer, lateral	K296	Q204	11 (11)	10 (11)
Crossover	Intra-dimer	K296	K296	N/A[c]	16 (14)
Crossover	Intra-dimer	Q204	Q204	17 (15)	15 (14)
Crossover	Inter-dimer, lateral	K296	A207	8 (10)	7 (9)
Crossover	Inter-dimer, lateral	A282	D221	N/A[c]	6 (6)
NN	Inter-dimer, longitudinal	E43	S74	12 (13)	7 (7)
NN	Inter-dimer, longitudinal	E57	E63	12 (14)	8 (9)
NN	Intra-monomer	E57	E63	11 (10)	12 (11)
CC	Inter-dimer, longitudinal	M443 (446)	M443 (446)	N/A[c]	12 (10)
CC	Intra-dimer	M443 (446)	M443 (446)	18 (16)	18 (17)
NC	Inter-dimer, longitudinal	R419 (422)	S34	N/A[c]	12 (12)
NC	Inter-dimer, longitudinal	R419 (422)	A37	N/A[c]	10 (9)

1021
1022 [a] Based on $CreS_{wt}$ numbering. Values in parentheses represent residue number based on $CreS_{sat}$
1023 numbering.
1024
1025 [b] Cβ-Cβ distance between two residues. Values in parentheses represent the Cα-Cα distance. For
1026 a given pair, the distance shown is the shortest among all equivalent pairs related by pseudo
1027 symmetry.
1028
1029 [c] At least one of the two residues is absent in the atomic model due to disorder or an ambiguity in
1030 model building.

1031 **SUPPLEMENTARY REFERENCES**

1032 1. Cabeen MT, Herrmann H & Jacobs-Wagner C (2011) The domain organization of the
1033 bacterial intermediate filament-like protein crescentin is important for assembly and
1034 function. *Cytoskeleton (Hoboken)* 68(4):205-219.
1035 2. Evinger M & Agabian N (1977) Envelope-associated nucleoid from *Caulobacter crescentus*
1036 stalked and swarmer cells. *J Bacteriol* 132(1):294-301.
1037 3. Gitai Z, Dye N & Shapiro L (2004) An actin-like gene can determine cell polarity in bacteria.
1038 *Proc Natl Acad Sci U S A* 101(23):8643-8648.
1039 4. Ingerson-Mahar M, Briegel A, Werner JN, Jensen GJ, & Gitai Z (2010) The metabolic
1040 enzyme CTP synthase forms cytoskeletal filaments. *Nat Cell Biol* 12(8):739-746.
1041 5. Cabeen MT, Charbon G, Vollmer W*, et al.* (2009) Bacterial cell curvature through
1042 mechanical control of cell growth. *EMBO J* 28(9):1208-1219.
1043 6. Modell JW, Kambara TK, Perchuk BS, & Laub MT (2014) A DNA damage-induced, SOS-
1044 independent checkpoint regulates cell division in *Caulobacter crescentus. PLoS Biol*
1045 12(10):e1001977.
1046 7. Rosenthal PB & Henderson R (2003) Optimal determination of particle orientation,
1047 absolute hand, and contrast loss in single-particle electron cryomicroscopy. *J. Mol. Biol.*
1048 333(4):721-745.
1049 8. Scheres SH & Chen S (2012) Prevention of overfitting in cryo-EM structure determination.
1050 *Nat. Methods* 9(9):853-854.
1051 9. Adams PD, Afonine PV, Bunkoczi G*, et al.* (2010) PHENIX: a comprehensive Python-
1052 based system for macromolecular structure solution. *Acta Crystallogr. D Biol. Crystallogr.*
1053 66(Pt 2):213-221.
1054 10. Afonine PV, Klaholz BP, Moriarty NW*, et al.* (2018) New tools for the analysis and
1055 validation of cryo-EM maps and atomic models. *Acta Crystallogr D Struct Biol* 74(Pt 9):814-
1056 840.
1057 11. Chen VB, Arendall WB, 3rd, Headd JJ*, et al.* (2010) MolProbity: all-atom structure
1058 validation for macromolecular crystallography. *Acta Crystallogr. D Biol. Crystallogr.* 66(Pt
1059 1):12-21.

1060
1061